A Unified Channel Model for IRS-Aided Underwater OWC with Combined Attenuation Losses

Yalçın Ata, *Senior Member, IEEE,* Xiang Yi, *Member, IEEE,*
Yuxuan Li, Xinyue Tao, and Anna Maria Vegni, *Senior Member, IEEE*

***Abstract*—In underwater environment, wireless signal propagation is very challenging, and strongly affected by absorption- and scattering-induced attenuation losses. Optical wireless communications (OWC), due to huge bandwidths, can provide high data rates and medium propagation ranges, representing a viable technology for underwater scenarios. There are several statistical distributions that model the effect of underwater turbulence on OWC, and how to model the underwater OWC (UOWC) channel with higher accuracy is still a topic to investigate. In this paper, we investigate the use of intelligent reflecting surfaces (IRSs) for enhancing performance in underwater OWC systems. In this regard, we present a unified channel model for UOWC, working both for heterodyne and intensity modulated/direct detection (IM/DD) schemes. The analytical expressions of average bit-error-rate (BER), outage probability, and channel capacity are derived including the combined effect of (*i*) attenuation, (*ii*) turbulence, (*iii*) pointing error, and (*iv*) angle-of-arrival (AOA) fluctuations to ensure the comprehensive characterization of underwater optical wireless communication channel. To make the analysis and results more realistic, the practical scenarios and parameters are considered. The probability density function (PDF) and the cumulative distribution function (CDF) of the underwater OWC channel are obtained analytically. Simulation results are presented for various parameters of underwater channel and communication systems. It is observed that the application of IRS remains as an important tool in terms of mitigating the overall fading effect caused by the combination of previous phenomena in underwater wireless channel. Also, the benefits of heterodyne detection over IM/DD is evinced.**

***Index Terms*—Intelligent reflecting surface (IRS), optical wireless channel, underwater optical wireless communication.**

I. Introduction

APPLICATION of intelligent reflecting surfaces (IRSs) has become a prominent candidate in terms of improving the performance of wireless communication systems particularly in fifth-generation (5G) and sixth-generation (6G) communication networks. Due to its re-configurable structure, energy conservation, and cost efficiency, the IRS application brings significant benefits such as implementation flexibility, easy deployment, utilization of the green wireless communication technology, and compatibility with the existing wireless communication networks.

Various studies have been devoted to characterizing the impact of IRS implementation on radio frequency (RF) communication. In [1], Liaskos *et al.* studied the IRS concept by using meta-surfaces capable of reflecting electromagnetic waves and surface units mounted in such a way so as to ensure the statistical independence of each reflected wave. It was shown that software controllable meta-surfaces have exceptional performance enhancement potential in wireless environments. In [2], Wu and Zhang presented an overview of IRS technology including application, hardware architecture, beam-forming design, trade-off between existing technologies, and new signal models. The integration of re-configurable meta-surfaces into wireless networks, practical challenges and limitations, algorithms and protocols in smart radio environments, possible artificial intelligence (AI)-based re-configurable meta-surfaces and interaction with the future 6G networks were discussed by Di Renzo *et al.* in [3]. The variations of the performance of wireless communication systems with the IRS application were also studied in various studies [4]–[8] according to different aspects. In [4] and [5], the IRS-based transmission was examined for wireless communication and a mathematical framework was constructed for bit-error-rate (BER) and symbol error rate (SER) for different modulated wireless communication systems. The benefit of IRS usage was shown, as well as the received signal-to-noise-ratio (SNR) boosts with the IRS application, thus making the communication reliable at low-SNR values. Karasik *et al.* [6] illustrated that besides the SNR maximizing IRS configuration, information encoding scheme at the transmitter also affects the channel capacity. In [7] Di Renzo *et al.* showed the superiority of sufficiently large IRSs over relay-assisted communication systems, as well as IRS reduction in implementation complexity. Another benefit of IRS application is the coverage extension that was investigated by Yang *et al.* in [8], by comparing with the relaying systems and direct transmission links.

Besides RF communications, the use of IRS for free space optical (FSO) communications has also attracted attention and has been analyzed in various studies. In [9], existing optical IRS technologies were investigated and the potential role of IRS application to overcome the line-of-sight (LoS) limitation was analyzed depending on mirror-based and meta-

Corresponding author: Anna Maria Vegni (E-mail: annamaria.vegni@uniroma3.it).

Y. Ata is with Department of Electrical and Electronics Engineering, OSTIM Technical University, OSTIM, 06374 Yenimahalle, Ankara, Turkey. (E-mail:ylcnata@gmail.com).

X. Yi, Y. X. Li and X. Y. Tao are with the School of Telecommunications Engineering, Xidian University, Xi'an, Shaanxi 710071, China (E-mail: yixiang@xidian.edu.cn, lyuxuan@stu.xidian.edu.cn, xyt@stu.xidian.edu.cn).

A. M. Vegni is with Department of Industrial, Electronics and Mechanical Engineering, Roma Tre University, Rome, Italy. (Email: annamaria.vegni@uniroma3.it).

surface-based technologies. Using a mirror-based IRS system in [10], the outage performance of an FSO system was calculated for both lognormal and Gamma-Gamma distributed turbulence channel including geometric and misalignment losses and attenuation. Another study [11] was carried out to indicate the influence of IRS on the performance of wireless communication systems operating in $\mathcal{F}-$distributed fading channel in terms of outage probability (OP) and average BER, including path loss and pointing errors. A novel geometric and misalignment loss (GML) model has been adopted by Sipani *et al.* in [12], in order to mitigate the effect of pointing error by means of IRS-aided FSO links.

All above mentioned mostly-theoretical studies revealed that IRS can improve the performance of both the FSO and the RF wireless communication systems significantly, and detailed further investigations are needed to have more comprehensive and more accurate characterization of IRS-aided wireless communication systems.

A. Related works

Due to rapidly growing number of applications in underwater medium from different industries, huge demand for noise immune, secure, high data rate and reliable communication has emerged and underwater optical wireless communication (UOWC) remains as the main solution to meet these requirements, while traditional acoustic communication is insufficient with very low data rate. However, optical beam is prone to be affected from underwater environment severely that limits the effective range of UOWC to several tens of meters. Several studies have investigated the closed-form expression for the average channel capacity of UOWC systems. In [13] Xu *et al.* exploit the Málaga fading model and its dependence on the link distance, the wavelength, the receiving aperture diameter, and other factors. Liu *et al.* [14] characterized an UOWC channel with both scattering/absorption and optical turbulence.

Based on the limitations caused by the chaotic nature of the underwater environment, the use of IRS should be evaluated the most for performance enhancement, as well as aperture averaging, adaptive optics correction, spatial diversity and power increase.

Although there are many studies available on the performance analysis of optical wireless communication (OWC) with IRS implementation in the atmospheric communication channel [9], there are not many studies on UOWC yet. In [15], both OP and average BER of hybrid UOWC/RF from underwater to terrestrial link were studied. However, IRS was implemented between terrestrial relay and FSO communication system, not in underwater medium. The general approach for IRS in underwater medium, IRS deployment types (*i.e.*, stationary and/or floating), IRS-equipped autonomous underwater vehicles (AUVs) and challenges were evaluated by Kisseleff *et al.* in [16] for different scenarios. In [17], Naik and Chung examined the OP, average BER and channel capacity including the underwater turbulence (with Nikishov's power spectrum), pointing error, and attenuation, which are modeled by Gamma-Gamma, Rayleigh and Beer-Lambert distributions, respectively. The Gamma-Gamma distribution has been adopted also in [18] to model a simple closed-form expression for the impulse response of UOWC links. Another study has been performed to analyze the influence of IRS on the performance of UOWC systems including the combined effect of turbulence, attenuation and pointing errors, [19]. Still on practical parameters of the underwater medium that can be encountered in the earth basins, the underwater turbulence power spectrum was selected as Oceanic Turbulence Optical Power Spectrum (OTOPS) model by Yao *et al.* in [20]. The authors also modeled the IRS-aided wireless communication channel by log-normal distribution, and the outage performance was presented for different water types. In [21], Lam *et al.* considered a realistic underwater scenario including the oceanic propagation loss, the oceanic turbulence, and pointing errors induced by IRS vibrations, while authors assumed that the IRS is installed under buoy or ships. The outcomes of this study reveal that the vibration of an IRS-installed under buoy/ship severely impacts the system outage performance. Recently, in [22], the benefit of IRS application has been analyzed for an exponential Weibull distributed channel together with the higher order beam usage including the effects of turbulence, pointing error and attenuation. The Weibull model has been adopted in [23] to characterize the fading of salinity in UOWC channels, and has shown an excellent match with the measured data under different channel conditions.

To the best of authors' knowledge, any study has not been reported that includes the combination of multiple attenuation and propagation phenomena such as absorption- and scattering-induced attenuation, turbulence, pointing error, and angle-of-arrival (AOA) fluctuations together with different detection schemes. We notice that the most relevant study to our analysis may be the analysis in [17]. However, our paper remains different according to the following items:

- In [17], the direct UOWC and IRS-assisted links are modeled by Gamma and Gamma-Gamma distributions, respectively, while we use the Gamma-Gamma distribution for both links.
- Authors in [17] use Nikishov's power spectrum model for turbulence parameters' calculations, while we use the OTOPS model utilizing the practical temperature and salinity concentration of underwater medium.
- Both studies use the Beer-Lambert's law to find the attenuation coefficient. However, we also find the absorption and scattering coefficients based on empirical model using chlorophyll concentration and wavelength.
- The study in [17] uses the Rayleigh model for pointing error, while we use the Hoyt distribution that permits asymmetric pointing error.
- Finally, the work in [17] does not take into account the AOA fluctuations, while our study covers the effect of AOA fluctuations with Rayleigh distribution.

The characterization of the combined effect of the aforementioned phenomena is relevant to get high approximation of underwater channel model with realistic parameters.

B. Main contributions

Motivated by the necessity of further and more comprehensive investigation of IRS application, we aim to investigate

the use of IRS for UOWC system under different joint attenuation factors. In order to mitigate the wireless communication channel effects, we investigate the outage, average BER and channel capacity performances of a UOWC system. The following items represent the main contributions of this paper, and are utilized to make our study as comprehensive as possible with realistic parameters:

- Section II-B, we investigate the combined effects of almost all possible phenomena that can be encountered in underwater medium such as underwater turbulence, pointing error, absorption- and scattering-induced attenuation loss, and AOA fluctuations for the modeling of an IRS-aided UOWC channel. The underwater turbulence spectrum is modeled by recently introduced OTOPS model that permits to use the practical values of average temperature and average salinity concentration.
- In Section III, we derive the unified channel probability density function (PDF) and cumulative density function (CDF) of SNR expressions that reduce to both intensity modulation direct detection (IM/DD) and heterodyne detection cases. The analytical expressions for both channel PDF and CDF are obtained depending on the Meijer-G function.
- In Section IV, the SNR-dependent OP, the average BER, and the channel capacity are derived in analytical expressions. The effects of the IRS element number and the reflection coefficients of surfaces are included in the PDF, CDF, OP, the average BER, as well as the channel capacity expressions.
- In Section V, the asymptotic approximations of OP and average BER for high SNR regime are obtained.
- In Section VI, the comparison of the performance achieved with heterodyne to those obtained with IM/DD detection scheme is carried out in terms of OP, the average BER, and achievable capacity, for different system and IRS parameters. The accuracy of the obtained results is verified with the Monte Carlo (MC) simulations.

This paper is organized as follows. The system and channel model for the proposed UOWC scenario is given in Section II, together with the model of the IRS-aided UOWC link. The unified channel PDF and CDF are illustrated in Sections III. From the expression of the CDF for the instantaneous SNR, the analytical derivations of OP, average BER and ergodic channel capacity are given in Sections IV. The asymptotic analysis of both OP and average BER is performed in Section V. The assessment of the proposed UOWC unified channel model is carried out through simulation results and related discussions in Section VI, while the concluding remarks are given in Section VII. The details of all derivations are finally given in dedicated Appendices.

II. System and Channel Models

A. System Model

The system model for IRS-aided UOWC system is represented in Fig. 1. A transmitter AUV and a receiver one are initially connected through an horizontal communication LoS link, but in case of blockages the IRS unit is deployed to redirect the signal from Tx AUV to Rx AUV, forming a non-line-of-sight (NLoS) link. The IRS includes $\mathcal{N}$ number of passive reflecting elements (with $\mathcal{N} \geq 1, \in \mathbb{N}^+$), each of them reflects the incident optical wave by adjusting the phase and amplitude with the help of a controller. The reflection coefficient of each IRS is β_r (*i.e.*, $\beta_r \in [0, 1]$). Notice that all the devices in the underwater scenario are assumed laying at the same quote h_Q [m] from the water surface, so that the communication links are horizontal.

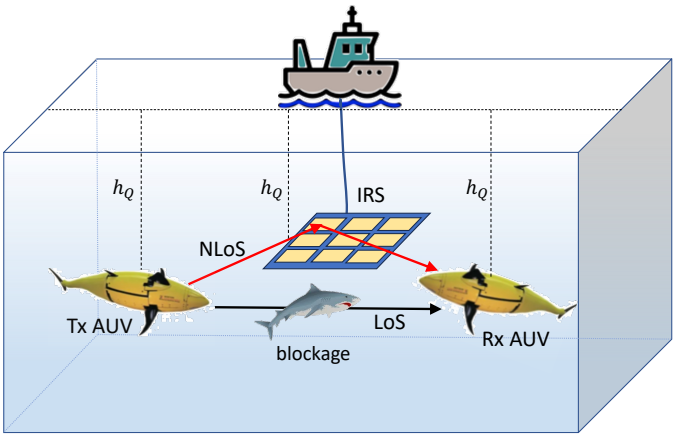

Fig. 1: System model for the IRS-aided UOWC system. A Tx AUV is in LoS with a Rx AUV (*black link*), but in case of blockages a NLoS link is established through the IRS unit (*red links*). The IRS is tethered to the boat. We also assume all the devices are at the same quote from the water surface, and then the communication links are horizontal.

The optical beam propagates in the underwater environment by exposure to the effects of absorption and scattering-dependent attenuation, turbulence, pointing error, and AOA fluctuations. The attenuation is calculated by using Beer-Lambert law. The underwater turbulence is modeled by recently introduced OTOPS model, and turbulent channel is assumed to have a Gamma-Gamma distribution. To see the effect of pointing error with different sizes in horizontal and vertical directions, we adopted the Hoyt distribution. Also, the beam deviations due to AOA fluctuations are obtained by using the Rayleigh model.

B. Channel Model

Including the combined effects of attenuation h_{al}, pointing error h_{pl}, turbulence h_{at}, and AOA fluctuations h_{af}, the total effective channel (*i.e.*, h) can be written as

$$h = h_{al} h_{at} h_{pl} h_{af}. \tag{1}$$

A short description of each component is provided as follows.

1) Absorption and Scattering: The attenuation h_{al} in underwater environment is usually the result of absorption and scattering, and strongly dependent on the wavelength of the optical beam, while absorption remains as the most dominant attenuating factor. The Beer-Lambert law describes the attenuation as

$$h_{al} = \exp[-c(\lambda) \cdot L], \tag{2}$$

where $c(\lambda)$ is the attenuation coefficient, λ [nm] is the beam wavelength, and L [m] is the wireless link length.

The attenuation coefficient can be written as the sum of absorption and scattering-induced attenuation coefficients as $c(\lambda) = a(\lambda) + b(\lambda)$. Specifically, the absorption coefficient $a(\lambda)$ is calculated by [24] as

$$\begin{aligned} a(\lambda) &= a_w(\lambda) + a_c^0(\lambda)\left(\frac{C_c}{C_c^0}\right)^{0.602} \\ &+ 62.6038 C_c \exp\left[0.12327\left(\frac{C_c}{C_c^0}\right)\right]\exp(-k_f\lambda) \\ &+ 3.6402 C_c \exp\left[0.12343\left(\frac{C_c}{C_c^0}\right)\right]\exp(-k_h\lambda), \end{aligned} \tag{3}$$

where $a_w(\lambda)$ [m^{-1}] is the absorption coefficient of pure water and it is empirically obtained in [25] for optically and chemically pure water, $a_c^0(\lambda)$ is the specific absorption coefficient of chlorophyll, C_c [$\mathrm{mg/m}^3$] is the total concentration of the chlorophyll, $C_c^0 = 1$ [$\mathrm{mg/m}]^3$ is the chlorophyll concentration, $k_f = 0.0189$ [nm^{-1}], and $k_h = 0.01105$ [nm^{-1}]. Waters are usually classified according to their chlorophyll concentrations and a widely used classification considers the following water types [26] *i.e.*, Jerlov-I with $C_c = 0.03$ [$\mathrm{mg/m}^3$], Jerlov-IA with $C_c = 0.1$ [$\mathrm{mg/m}^3$], Jerlov-IB with $C_c = 0.4$ [$\mathrm{mg/m}^3$], Jerlov-II with $C_c = 1.25$ [$\mathrm{mg/m}^3$], and Jerlov-III with $C_c = 3$ [$\mathrm{mg/m}^3$].

Also, in Eq. (2) the scattering coefficient $b(\lambda)$ is given in [24] by

$$\begin{aligned} b(\lambda) &= 0.005826(400/\lambda)^{4.322} \\ &+ 0.02(400/\lambda)^{1.7} C_c \exp[0.11631(C_c/C_c^0)] \\ &+ 0.2602(400/\lambda)^{0.3} C_c \exp[0.03092(C_c/C_c^0)]. \end{aligned} \tag{4}$$

It should be noted that the scattering-induced effect can be considered as random variable. In [27], the scattering-induced fading was modeled by Gamma distribution. However, since there are limitations related to distance and water types, we adopt the use of the traditional deterministic scattering model that is verified experimentally.

2) Underwater Turbulence: The PDF of Gamma-Gamma distributed turbulence channel h_{at} is expressed as [28]

$$f_{h_{at}}(h_{at}) = \frac{2(\alpha\beta)^{\frac{(\alpha+\beta)}{2}}}{\Gamma(\alpha)\Gamma(\beta)} h_{at}^{\frac{(\alpha+\beta)}{2}-1} K_{\alpha-\beta}\left(2\sqrt{\alpha\beta h_{at}}\right), \tag{5}$$

where $h_{at} > 0$, $K_a(\cdot)$ is the modified Bessel function with order a, $\alpha = [\exp(\sigma^2_{\ln X}) - 1]^{-1}$, and $\beta = [\exp(\sigma^2_{\ln Y}) - 1]^{-1}$. The $\sigma^2_{\ln X}$ and $\sigma^2_{\ln Y}$ indicate the effects of large and small turbulent scales and they are calculated respectively by [28, pp.352]

$$\sigma^2_{\ln X} = \frac{0.49\sigma_B^2}{\left[1 + 0.56(1+\Theta_1)\sigma_B^{12/5}\right]^{7/6}}, \tag{6}$$

and

$$\sigma^2_{\ln Y} = \frac{0.51\sigma_B^2}{\left(1 + 0.69\sigma_B^{12/5}\right)^{5/6}}, \tag{7}$$

where σ_B^2 is the Rytov variance of the Gaussian beam, whose expression is given in Appendix A, $\Theta_1 = \Theta_0/(\Theta_0^2 + \Lambda_0^2)$ [m] as the beam curvature parameter at the receiver, with Θ_0 as the parameter of beam curvature at the transmitter, $\Lambda_0 = 2L/kW_0^2$, W_0 [m] is the beam radius, $\Theta_0 = 1 - L/F_0$ is the parameter of beam curvature at the transmitter, and F_0 [m] is the curvature's phase front radius. Notice that in order to model the wireless optical propagation in a realistic underwater environment, we use the OTOPS model, as it exploits the practical values of the water parameters. In Appendix A we show that the Rytov variance of the Gaussian beam is affected by the average temperature, the average salinity of the water, and the co-spectra.

Since we are using IRS application, assuming that we have a number of $\mathcal{N}$ surfaces, then the sum of Gamma-Gamma random variables can be expressed by a new Gamma-Gamma random variable [29] and the PDF takes the form of

$$f_{h_{at}}(h_{at}) = \frac{2\left(\frac{\alpha_s\beta_s}{\mathcal{N}}\right)^{\frac{(\alpha_s+\beta_s)}{2}} h_{at}^{\frac{(\alpha_s+\beta_s)}{2}-1}}{\Gamma(\alpha_s)\Gamma(\beta_s)} K_v\left(2\sqrt{\frac{\alpha_s\beta_s}{\mathcal{N}}h_{at}}\right), \tag{8}$$

where $v = \alpha_s - \beta_s$, with α_s and β_s expressed respectively as

$$\alpha_s = \mathcal{N}\alpha + (\mathcal{N}-1)\frac{(-0.127 - 0.95\alpha - 0.0058\beta)}{(1 + 0.00124\alpha + 0.98\beta)}, \tag{9}$$

$$\beta_s = \mathcal{N}\beta. \tag{10}$$

3) Pointing error: The PDF of pointing error with asymmetrical deviations –different in vertical and horizontal directions– is given in polar coordinates by Hoyt distribution as [30]

$$f_{r,\varphi}(r,\varphi) = \frac{r}{2\pi q_H \sigma_s^2}\exp\left[-\frac{r^2\xi(\varphi)}{2\sigma_s^2}\right], \tag{11}$$

where $q_H = \sigma_z/\sigma_s, \in (0,1]$, with σ_s and σ_z as the beam deviations in orthogonal $s = r\cos(\varphi)$ and $z = r\sin(\varphi)$ directions, respectively, and $\xi(\varphi)$ is given as

$$\xi(\varphi) = \left[1 - (1 - q_H^2)\cos^2\varphi\right]/q_H^2. \tag{12}$$

Using Eqs. (11) and (12), the PDF of misalignment is found in integral form in [30] by

$$f_{h_{pl}}(h_{pl}) = \frac{\eta_s^2}{2\pi q_H}\int_{-\pi}^{\pi} \frac{h_{pl}^{\eta_s^2\xi(\varphi)-1}}{A_0^{\eta_s^2\xi(\varphi)}}\mathrm{d}\varphi, \quad 0 \le h_{pl} \le A_0 \tag{13}$$

where $\eta_s = \omega_e/(2\sigma_s)$, with $\omega_e = \omega_b\sqrt{\sqrt{\pi}\mathrm{erf}(\varrho)/(2\varrho e^{-\varrho^2})}$, and ω_b as the beamwaist. Also, $\mathrm{erf}(\cdot)$ is the error function, $\varrho = \sqrt{\frac{\pi r_a^2}{2\omega_b^2}}$, r_a [m] is the receiver aperture radius, $D_G = 2\times r_a$ [m] is the receiver aperture diameter, and $A_0 = \mathrm{erf}^2(\varrho)$.

4) AOA Fluctuations: In underwater environment, as well as atmospheric medium, AOA fluctuations often result from a large number of turbulent eddies and random perturbations [31]. For a circular receiver aperture, the fraction of the power onto the photodetector follows Airy pattern consisting of main-lobe and side-lobes. It was shown in [32] that almost all the power of the Airy pattern (*e.g.*, $\geq 99\%$) is included in the circle with radius of 25λ and the main-lobe width is approximately equal to 2.4λ, and both values are much smaller than the size of photodetector radius. The power loss

due to AOA fluctuations h_{af}, which can also be called to link interruption parameter (since link is interrupted when AOA fluctuations of optical beam fall outside the field-of-view (FoV)), will take discrete values "1" and "0" indicating that the received optical beam is inside the FoV or not, respectively. The effect of side-lobes remains small and does not yield an error therefore, ignoring the side-lobes effect, the link interruption parameter can be expressed by [33]

$$h_{af} = \begin{cases} 1 & \text{if} \quad \theta_d \leq \theta_{FOV} \\ 0 & \text{if} \quad \theta_d > \theta_{FOV}, \end{cases} \tag{14}$$

where θ_d is the incidence angle relative to the receiver axis that shows the random orientation deviations at the receiver plane. Following Eq. (14), we can utilize the PDF of random variable θ_d, showing the AOA fluctuations, expressed by Rayleigh distribution *i.e.*, [33]

$$f_{\theta_d}(\theta_d) = \frac{\theta_d}{\sigma_0^2} \exp\left(-\frac{\theta_d^2}{2\sigma_0^2}\right), \tag{15}$$

where $\theta_d \geq 0$ and σ_0^2 represents the variance of θ_d.

C. Signal Model for IRS-Aided UOWC Link

A signal sent from the transmitting AUV, and reflected from the IRS, will reach the receiver AUV with the following expression [5]

$$y = \left[\sum_{n=1}^{\mathcal{N}} h_1 \beta_{rn} e^{j\theta_n} h_2\right] x + n_0, \tag{16}$$

where x is the transmitted signal, $h_1 = g_n e^{-j\phi_n}$ is the path gain for the first link connecting the Tx AUV to the n-th IRS element (where g_n refers to the amplitude of the link gain and ϕ_n is the phase shift of the transmitted signal from the Tx AUV impinging the n-th IRS element), and $h_2 = u_n e^{-j\varphi_n}$ indicates the path gain for the second link connecting the n-th IRS element to the Rx AUV (where u_n refers to the amplitude of the link gain and φ_n is the phase shift of the transmitted signal from the n-th IRS element to the Rx AUV), $\beta_{rn} \in [0, 1]$ is the reflection coefficient of the n-th reflecting element of the IRS (with $n = 1, \ldots, \mathcal{N}$), $\theta_n \in [0, 2\pi]$ is the phase shift caused by the n-th reflecting element, and n_0 is the additive white Gaussian noise (AWGN) with zero mean and variance σ_n^2. By setting $\theta_n = \phi_n + \varphi_n$ in order to maximize the SNR, the received signal becomes

$$y = \sum_{n=1}^{\mathcal{N}} g_n \beta_{rn} u_n x + n_0. \tag{17}$$

Assuming that all the reflecting elements of the IRSs are identical with same reflection coefficient *i.e.*, $\beta_{rn} = \beta_r$, in case of heterodyne detection scheme the instantaneous electrical SNR will take the form of

$$\gamma = \left(\sum_{n=1}^{\mathcal{N}} h_n\right) \beta_r P_t / \sigma_n^2, \tag{18}$$

where P_t is the average transmitted electrical power. Eq. (18) leads the instantaneous SNR as $\gamma = \overline{\gamma} h / \mathbb{E}[h]$, where $\overline{\gamma}$ is the average SNR defined as $\overline{\gamma} = \mathbb{E}[h]\beta_r P_t / \sigma_n^2$ for heterodyne detection, and $h = \sum_{n=1}^{\mathcal{N}} h_n$ is the combined total effective channel (where h_n is the attenuation of the n-th effective channel and it can be expressed by $h_n = h_{al_n} h_{at_n} h_{pl_n} h_{af_n}$ according to the channel model given in Eq. (1)), with $h_n = g_n u_n$. On the other hand, using IM/DD scheme, the instantaneous SNR becomes

$$\gamma = \left(\sum_{n=1}^{\mathcal{N}} h_n\right)^2 \beta_r^2 P_t^2 / \sigma_n^2, \tag{19}$$

that yields the instantaneous SNR as $\gamma = \overline{\gamma} h^2 / \mathbb{E}[h^2]$, where $\overline{\gamma} = \mathbb{E}[h^2]\beta_r^2 P_t^2 / \sigma_n^2$ is the average SNR for IM/DD detection. Finally, combining Eq. (18) and (19), and unifying the power-dependent expressions of the average SNR *i.e.*, $\overline{\gamma} = \mathbb{E}[h^r]\beta_r^r P_t^r / \sigma_n^2$, the unified instantaneous SNR can be written by

$$\gamma = \overline{\gamma} h^r, \tag{20}$$

where $r = 1$ and $r = 2$ correspond to heterodyne and IM/DD detection schemes, respectively. Without loss of generality, we have normalized the expected value $\mathbb{E}[h^r]$ to unity which allows us to focus on the effects of other parameters without the added complexity of channel gain variability.

III. Unified UOWC Channel Function Analysis

In Eq. (1), the term h_{af} represents the link interruptions resulting from AOA fluctuations at the receiver plane [33] and it behaves like a filter having values "1" and "0". The angle of the radial displacement vector between the optical beam axis and the center of receiver plane *i.e.*, the orientation deviation θ_d, results in pointing error loss on the beam intensity multiplied by $\cos\theta_d$. The angle θ_d causes the conditioned PDF of h_{pl} as $h_{pl|\theta_d}$. Given that the attenuation h_{al} is deterministic, while turbulence h_{at} and pointing error h_{pl} are probabilistic, and also defining $h_{ag} = h_{al} h_{at} h_{pl}$, the PDF of h_{ag} can be conditioned over θ_d *i.e.*,

$$\begin{aligned} f_{h_{ag}|\theta_d}(h_{ag}) &= \int f_{h_{ag}|\theta_d, h_{at}}(h_{ag}) f_{h_{at}}(h_{at}) \mathrm{d}h_{at} \\ &= \int_{\Delta_l}^{\infty} \frac{f_{h_{at}}(h_{at})}{h_{al} h_{at}} f_{h_{pl}|\theta_d}\left(\frac{h_{ag}}{h_{al} h_{at}}\right) \mathrm{d}h_{at}, \end{aligned} \tag{21}$$

where $\Delta_l = h_{ag} / (A_0 h_{al} \cos\theta_d)$. It is worth mentioning how Δ_l is obtained here. The validity range of h_{pl} becomes $[0, A_0 \cos\theta_d]$ after conditioned on θ_d. Using the relationship $h_{ag} = h_{al} h_{at} h_{pl}$, the upper bound h_{pl} can be written as $h_{pl} = \frac{h_{ag}}{h_{al} h_{at}} \leq A_0 \cos\theta_d$. Since Eq. (21) is over h_{at}, the lower bound of h_{at} can be taken out as $h_{at} \geq \frac{h_{ag}}{h_{al} A_0 \cos\theta_d}$, which we call Δ_l. Also, since we define $h_{ag} = h_{al} h_{at} h_{pl}$ for mathematical analysis, it should be noted that $f_{h_{ag}|\theta_d}(h_{ag})$ does not include the effect of h_{af} that is used to build the expression of the PDF of the total channel given in Eq. (B.4). In Eq. (21), the conditional PDF $f_{h_{pl}|\theta_d}(h_{pl})$, with $\frac{h_{ag}}{h_{al} h_{at}} = h_{pl}$, will be

$$f_{h_{pl}|\theta_d}(h_{pl}) = \frac{\eta_s^2}{2\pi q_H} \int_{-\pi}^{\pi} \frac{h_{pl}^{\eta_s^2 \xi(\varphi) - 1}}{(A_0 \cos\theta_d)^{\eta_s^2 \xi(\varphi)}} \mathrm{d}\varphi. \tag{22}$$

Using the derivation steps given in Appendix B, the PDF of the combined total effective channel will be obtained as

$$f_h(h) = \frac{\eta_s^2\left[1-\exp\left(-\frac{\theta_{FOV}^2}{2\sigma_0^2}\right)\right]}{2\pi q_H \Gamma(\alpha_s)\Gamma(\beta_s)} h^{-1} \int_{-\pi}^{\pi} \mathrm{d}\varphi \times G_{1,3}^{3,0}\left(\frac{\alpha_s\beta_s h}{\mathcal{N}A_0 h_{al}}\middle| \begin{matrix} 1+\eta_s^2\xi(\varphi) \\ \eta_s^2\xi(\varphi),\alpha_s,\beta_s \end{matrix}\right) + \delta(h)\exp\left(-\frac{\theta_{FOV}^2}{2\sigma_0^2}\right), \tag{23}$$

where $G_{p,q}^{m,n}(\cdot)$ and $\delta(\cdot)$ are the Meijer's-G and Dirac-delta functions, and θ_{FOV} is the FoV. The unified PDF of instantaneous SNR γ can be found by using the relationships given in Eq. (20) *i.e.*,

$$f_\gamma(\gamma) = f_h\left(\sqrt[r]{\frac{\gamma}{\overline{\gamma}}}\right)\left|\frac{\mathrm{d}h}{\mathrm{d}\gamma}\right|, \tag{24}$$

which can be rewritten as

$$f_\gamma(\gamma) = \frac{\eta_s^2\left[1-\exp\left(-\frac{\theta_{FOV}^2}{2\sigma_0^2}\right)\right]}{2r\pi q_H \Gamma(\alpha_s)\Gamma(\beta_s)} \int_{-\pi}^{\pi} \mathrm{d}\varphi \times \gamma^{-1} G_{1,3}^{3,0}\left(\frac{\alpha_s\beta_s}{\mathcal{N}A_0 h_{al}}\left(\frac{\gamma}{\overline{\gamma}}\right)^{\frac{1}{r}}\middle| \begin{matrix} 1+\eta_s^2\xi(\varphi) \\ \eta_s^2\xi(\varphi),\alpha_s,\beta_s \end{matrix}\right) + \frac{1}{r\overline{\gamma}^{\frac{1}{r}}\gamma^{1-\frac{1}{r}}}\delta\left[\left(\frac{\gamma}{\overline{\gamma}}\right)^{\frac{1}{r}}\right]\exp\left(-\frac{\theta_{FOV}^2}{2\sigma_0^2}\right). \tag{25}$$

Notice that Eq. (25) represents the analytical expression of channel PDF, which changes in a closed-form in case of $q_H = 1$. This consideration applies also to the analytical expressions related to the BER, OP, and the channel capacity, derived in the following section.

The CDF of the instantaneous SNR can be obtained by using the following expression *i.e.*,

$$F_\gamma(\gamma) = \int_0^\gamma f_\gamma(x)\mathrm{d}x, \tag{26}$$

which, after some derivations given in Appendix C, becomes

$$F_\gamma(\gamma) = \frac{\eta_s^2\left[1-\exp\left(-\frac{\theta_{FOV}^2}{2\sigma_0^2}\right)\right]}{2\pi q_H \Gamma(\alpha_s)\Gamma(\beta_s)} \int_{-\pi}^{\pi} \mathrm{d}\varphi \times G_{2,4}^{3,1}\left(\frac{\alpha_s\beta_s}{\mathcal{N}A_0 h_{al}}\left(\frac{\gamma}{\overline{\gamma}}\right)^{\frac{1}{r}}\middle| \begin{matrix} 1,1+\eta_s^2\xi(\varphi) \\ \eta_s^2\xi(\varphi),\alpha_s,\beta_s,0 \end{matrix}\right) + \exp\left(-\frac{\theta_{FOV}^2}{2\sigma_0^2}\right) H\left[\left(\frac{\gamma}{\overline{\gamma}}\right)^{\frac{1}{r}}\right], \tag{27}$$

where $H(\cdot)$ is the Heaviside function.

IV. Performance Metric Derivations

From the expression of the CDF of SNR, the outage probability OP, which is defined as the probability of instantaneous SNR being lower than the defined threshold SNR, can be found by

$$P_{out} = \Pr(\gamma \le \gamma_{th}) = F_\gamma(\gamma_{th}). \tag{28}$$

Substituting Eq. (27) into Eq. (28), the OP of IRS-aided UOWC link will be in analytical form as

$$P_{out} = \frac{\eta_s^2\left[1-\exp\left(-\frac{\theta_{FOV}^2}{2\sigma_0^2}\right)\right]}{2\pi q_H \Gamma(\alpha_s)\Gamma(\beta_s)} \int_{-\pi}^{\pi} \mathrm{d}\varphi \times G_{2,4}^{3,1}\left(\frac{\alpha_s\beta_s}{\mathcal{N}A_0 h_{al}}\left(\frac{\gamma_{th}}{\overline{\gamma}}\right)^{\frac{1}{r}}\middle| \begin{matrix} 1,1+\eta_s^2\xi(\varphi) \\ \eta_s^2\xi(\varphi),\alpha_s,\beta_s,0 \end{matrix}\right) + \exp\left(-\frac{\theta_{FOV}^2}{2\sigma_0^2}\right). \tag{29}$$

A unified BER expression that permits to evaluate different types of modulation was obtained in [34]

$$P_e = \frac{\delta_x}{2\Gamma(p)} \sum_{l=1}^{n_x} \int_0^\infty \Gamma(p, q_l\gamma) f_\gamma(\gamma)\mathrm{d}\gamma, \tag{30}$$

where $\Gamma(a,b)$ is the upper incomplete Gamma function and the parameters p, δ_x, n_x and q_l are given for different modulation types in TABLE I, whose values come from [34]. Following the derivations given in Appendix D, the average BER can be found as

$$P_e = \frac{r^{\alpha_s+\beta_s-2}\delta_x\eta_s^2\left[1-\exp\left(-\theta_{FOV}^2/2\sigma_0^2\right)\right]}{2(2\pi)^r q_H \Gamma(\alpha_s)\Gamma(\beta_s)\Gamma(p)} \int_{-\pi}^{\pi} \mathrm{d}\varphi \sum_{l=1}^{n_x} \times G_{r+2,3r+1}^{3r,2}\left(\Delta_x\middle| \begin{matrix} 1,1-p,\Delta(1+\eta_s^2\xi(\varphi):r) \\ \Delta(\eta_s^2\xi(\varphi):r),\Delta(\alpha_s:r),\Delta(\beta_s:r),0 \end{matrix}\right) + \frac{n_x\delta_x}{2}\exp\left(-\frac{\theta_{FOV}^2}{2\sigma_0^2}\right), \tag{31}$$

where $\Delta_x = [\alpha_s\beta_s/(\mathcal{N}A_0 h_{al} r^2 q_l^{\frac{1}{r}}\overline{\gamma}^{\frac{1}{r}})]^r$ and $\Delta(y:x) = \frac{y}{x}, \frac{y+1}{x}, \ldots, \frac{y+x-1}{x}$.

Finally, according to [35], the unified expression for channel capacity including both heterodyne and IM/DD detection schemes can be written by

$$\overline{C} \triangleq \mathbb{E}\left[\log_2(1+c_r\gamma)\right] = \frac{1}{\ln 2}\int_0^\infty \ln(1+c_r\gamma) f_\gamma(\gamma)\mathrm{d}\gamma, \tag{32}$$

where $\mathbb{E}[\cdot]$ denotes the mean value, and $c_r = \left\{1, \frac{e}{2\pi}\right\}$ for heterodyne (*i.e.*, $r=1$) and IM/DD (*i.e.*, $r=2$) detection schemes, respectively. Based on derivations given in Appendix E, the ergodic channel capacity is found to be

$$\overline{C} = \frac{r^{\alpha_s+\beta_s-2}\eta_s^2\left[1-\exp\left(-\theta_{FOV}^2/2\sigma_0^2\right)\right]}{\ln 2(2\pi)^r q_H \Gamma(\alpha_s)\Gamma(\beta_s)} \int_{-\pi}^{\pi} \mathrm{d}\varphi \times G_{r+2,3r+2}^{3r+2,1}\left(\Delta_z\middle| \begin{matrix} 0,1,\Delta(1+\eta_s^2\xi(\varphi):r) \\ \Delta(\eta_s^2\xi(\varphi):r),\Delta(\alpha_s:r),\Delta(\beta_s:r),0,0 \end{matrix}\right), \tag{33}$$

where $\Delta_z = [\alpha_s\beta_s/(A_0 h_{al} r^2 \mathcal{N} c_r^{\frac{1}{r}}\overline{\gamma}^{\frac{1}{r}})]^r$ and $\Delta(y:x) = \frac{y}{x}, \frac{y+1}{x}, \ldots, \frac{y+x-1}{x}$.

TABLE I: Parameters in Eq. (30) for different modulation scheme, [34].

Modulation Scheme	Detection Type	p	δ_x	n_x	q_l
BPSK	Heterodyne	$1/2$	1	1	1
M-PSK		$1/2$	$\frac{2}{\max(\log_2 M,2)}$	$\max\left(\frac{M}{4},1\right)$	$\sin^2\left(\frac{(2l-1)\pi}{M}\right)\log_2 M$
M-QAM		$1/2$	$\frac{4}{\log_2 M}\left(1-\frac{1}{\sqrt{M}}\right)$	$\frac{\sqrt{M}}{2}$	$\frac{3(2l-1)^2}{2(M-1)}\log_2 M$
OOK	IM/DD	$1/2$	1	1	$1/2$

V. Asymptotic Analysis

Asymptotic expressions generally simplify complex mathematical formulations, making them more tractable, especially in high SNR conditions where exact expressions are challenging to handle. They provide valuable insights into the fundamental behavior and limitations of optical wireless communication systems, helping to identify key factors that dominate performance in high SNR regimes. Since achieving a high SNR is crucial for reliable UOWC, we will give the variation of the OP and the average BER performance in high SNR regime by approximating the analytical solutions.

A. Outage Probability

According to the derivations given in Appendix F, the asymptotic expansion of OP is found to be:

$$P_{out_{\overline{\gamma}\gg 1}} = \frac{\eta_s^2\left[1-\exp\left(-\frac{\theta_{FOV}^2}{2\sigma_0^2}\right)\right]}{2\pi q_H\Gamma(\alpha_s)\Gamma(\beta_s)}\int_{-\pi}^{\pi}\left(\sum_{j=1}^{3}\Upsilon_j\overline{\gamma}^{-\theta_j}\right)\mathrm{d}\varphi + \exp\left(-\frac{\theta_{FOV}^2}{2\sigma_0^2}\right), \tag{34}$$

where

$$\Upsilon_1 = \frac{\Gamma(\alpha_s-\eta_s^2\xi(\varphi))\Gamma(\beta_s-\eta_s^2\xi(\varphi))}{\eta_s^2\xi(\varphi)}\left(\frac{\alpha_s\beta_s\gamma_{th}^{\frac{1}{r}}}{\mathcal{N}A_0h_{al}}\right)^{\eta_s^2\xi(\varphi)}, \tag{35}$$

$$\Upsilon_2 = \frac{\Gamma(\beta_s-\alpha_s)}{\alpha_s(\eta_s^2\xi(\varphi)-\alpha_s)}\left(\frac{\alpha_s\beta_s\gamma_{th}^{\frac{1}{r}}}{\mathcal{N}A_0h_{al}}\right)^{\alpha_s}, \tag{36}$$

$$\Upsilon_3 = \frac{\Gamma(\alpha_s-\beta_s)}{\beta_s(\eta_s^2\xi(\varphi)-\beta_s)}\left(\frac{\alpha_s\beta_s\gamma_{th}^{\frac{1}{r}}}{\mathcal{N}A_0h_{al}}\right)^{\beta_s}, \tag{37}$$

and

$$\theta_j = \left\{\frac{\eta_s^2\xi(\varphi)}{r}, \frac{\alpha_s}{r}, \frac{\beta_s}{r}\right\}. \tag{38}$$

B. Average BER

According to the procedures given in Appendix F, the asymptotic expression of the average BER in high SNR regime can be obtained as

$$P_{e_{\gamma\gg 1}} = \frac{r^{\alpha_s+\beta_s-3}\delta_x\eta_s^2\left[1-\exp\left(-\theta_{FOV}^2/2\sigma_0^2\right)\right]}{2(2\pi)^r q_H\Gamma(\alpha_s)\Gamma(\beta_s)\Gamma(p)} \times\int_{-\pi}^{\pi}\sum_{l=1}^{n_x}\sum_{j=1}^{3r}\left(h_j^{\dagger}\Delta_y^{\frac{b_j}{\beta_j}}\right)\mathrm{d}\varphi + \frac{n_x\delta_x}{2}\exp\left(-\frac{\theta_{FOV}^2}{2\sigma_0^2}\right), \tag{39}$$

where $\Delta_y = [\alpha_s\beta_s/(A_0h_{al}r^2\mathcal{N}q_l^{\frac{1}{r}}\overline{\gamma}^{\frac{1}{r}})]$, and b_j, β_j are defined in Appendix F.

TABLE II: Parameters adopted in the simulation results.

Symbol	Value	Symbol	Value
λ	417 nm	$\langle T\rangle$	20 °C
L	40 m	$\langle S\rangle$	30 ppt
W_0	1 mm	H	-0.2 °C.ppt^{-1}
F_0	∞	q_H	0.7
D_G	1 cm	ω_b	$5\times r_a$
θ_{FOV}	70 mrad	σ_0	12 mrad
$\overline{\gamma}$	40 dB	σ_s	$1\times r_a$
γ_{th}	2 dB	C_c	0.03 mg/m^3
ε	10^{-5} m^2/s^3	$\mathcal{N}$	10
χ_T	10^{-5} K^2/s	β_r	0.8

VI. Results and Discussion

This section provides both analytical and asymptotic results the OP, the average BER, and the ergodic channel capacity of an IRS-aided UOWC system. Results have been carried out both for heterodyne and IM/DD detection schemes, for various parameters. The accuracy of the obtained results is verified by using MC simulations with a set of $[10^6, 10^9]$ realizations. The chosen environmental, beam and system parameters are given in TABLE II, while any different parameters are given in either figure captions or in the figures. Since violet-blue region of the visible light spectrum presents the lowest absorption effect (*i.e.*, highest transmissivity) in underwater medium, the wavelength of the optical beam is selected as $\lambda = 417$nm. While the optimum distance is around $L \sim 10-20$m, we consider a longer distance as $L = 40$m to observe the

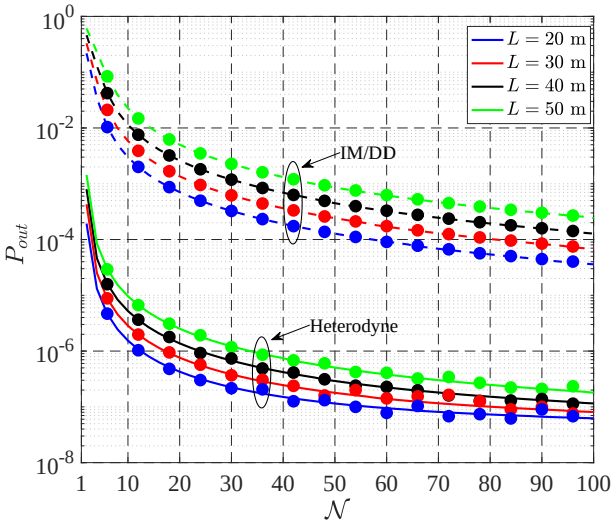

Fig. 2: OP variation versus the number of IRS elements and different link lengths, in case of (*i*) IM/DD (*dashed lines*) and (*ii*) heterodyne detection schemes (*solid lines*). Circle markers refer to MC simulations.

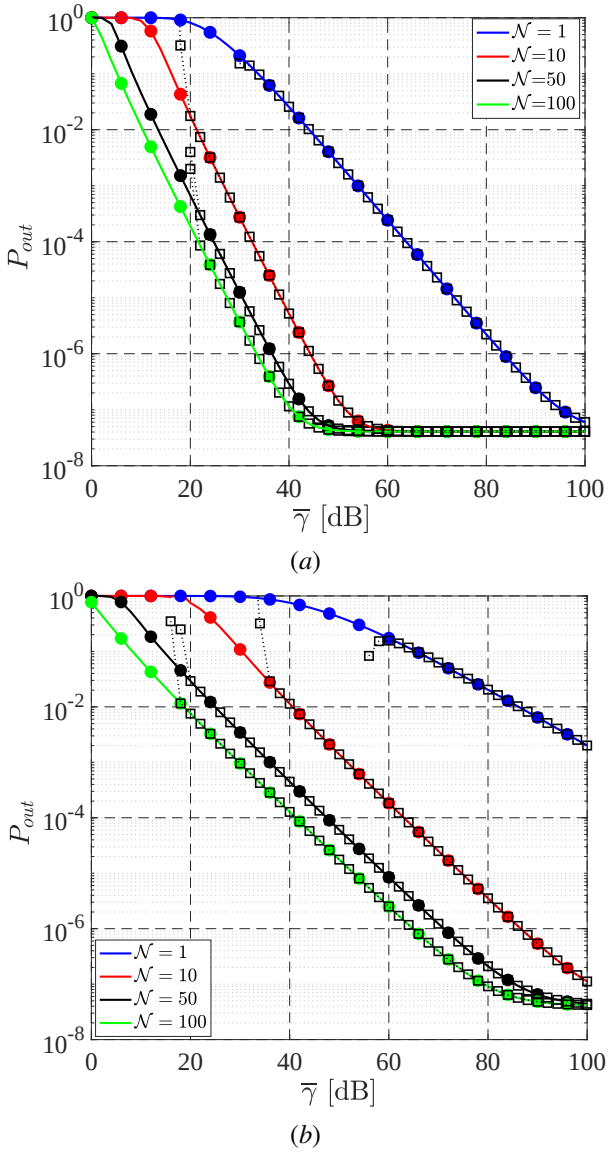

Fig. 3: OP variation versus the average SNR for different values of the number of IRS elements, in case of (*a*) heterodyne and (*b*) IM/DD detection schemes. Circle and square markers refer to MC simulations and asymptotic trend, respectively.

benefit of IRS at challenging conditions. The energy and temperature dissipation rates, the average temperature and salinity concentrations are selected for their moderate levels as $\varepsilon = 10^{-5}$ m^2/s^3, $\chi_T = 10^{-5}$ K^2/s, $\langle T \rangle = 20°$C, and $\langle S \rangle = 30$ ppt, respectively, which represent typical values in underwater medium [26]. To avoid the larger beam divergence, Gaussian beam is selected to be collimated and narrow having $W_0 = 1$ mm radius. Chlorophyll concentration is selected for the Jerlov-I water as $C_c = 0.03$ mg/m^3 which corresponds to the clear water. Due to the challenging nature of the underwater medium, the required average SNR for optimum performance metrics remains high therefore the average SNR is chosen at high level as $\overline{\gamma} = 40$ dB.

We assume each element of the IRS is sufficiently large and statistically independent to reflect the incoming optical signals effectively. This assumption is based on typical practical deployments where IRS sizes are designed to cover a significant area for effective signal manipulation. In most recent works it is assumed that the entire IRS is illuminated by the beam of the transmitter. Indeed, due to the electrically-large size of the IRS at optical frequencies, the reflected wave can often be modeled as a narrow beam. However, as the optical intensity of the transmitter increases, the beamwidth becomes narrower and the footprint on the IRS becomes smaller. With increasing intensity, the IRS area is only partly utilized, consequently affecting the desired received intensity [36]. In [10], it was expressed that the beam reflected by the IRS is a truncated Gaussian beam, whose width depends on the angles of incident and reflection and is confined to a truncation region, outside of which the reflected optical power is negligible. The required IRS size to avoid the beam truncation is dependent on the laser beam size and the sways of platforms on which transmitter and IRS are mounted. In case of beam truncation by the IRS surface, the incident optical intensity residing beyond the IRS area cannot be captured by the IRS, leading effectively to intensity loss. A common assumption in the literature is an IRS with dimensions of tens of cm or larger will be sufficient to avoid beam truncation [10]. For larger IRSs, some parts of the IRS are not illuminated with significant optical power, and therefore, do not contribute to the received signal. To give a practical example, assuming an IRS of 10 cm×10 cm size, comprised of $\mathcal{N} = 100$ elements, then a single element (*i.e.*, $\mathcal{N} = 1$) means it has a size of 10^{-4} m^2.

Fig. 2 illustrates the achieved OP in case of an IRS-aided UOWC system working in heterodyne (*solid lines*) and IM/DD (*dashed lines*), versus the number of IRS elements and for different link lengths. It is revealed that the performance of the outage probability improves with the application of IRS, and also increases with the number of IRS elements. While the OPs for both heterodyne and IM/DD detections decrease quickly until a certain value of IRS number, *e.g.*, $\mathcal{N} \sim 50$, then the decrease of OP for both detection types becomes slower with the increase of the number of IRS elements. It follows

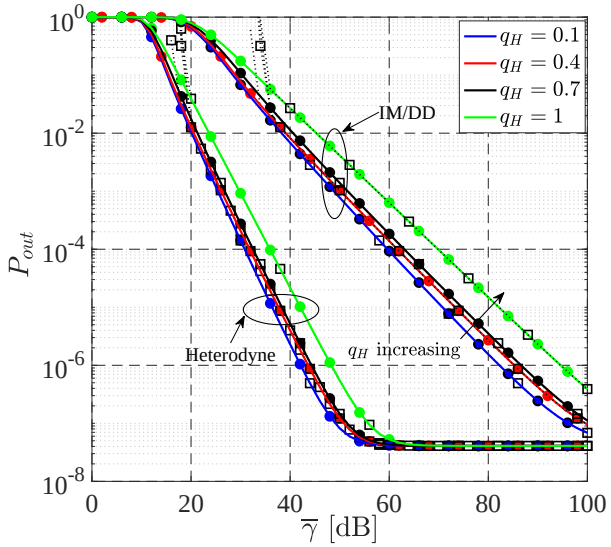

Fig. 4: OP variation versus the average SNR for different values of the beam asymmetry ratio q_H, in case of IM/DD and heterodyne detection schemes. Circle and square markers refer to MC simulations and asymptotic trend, respectively.

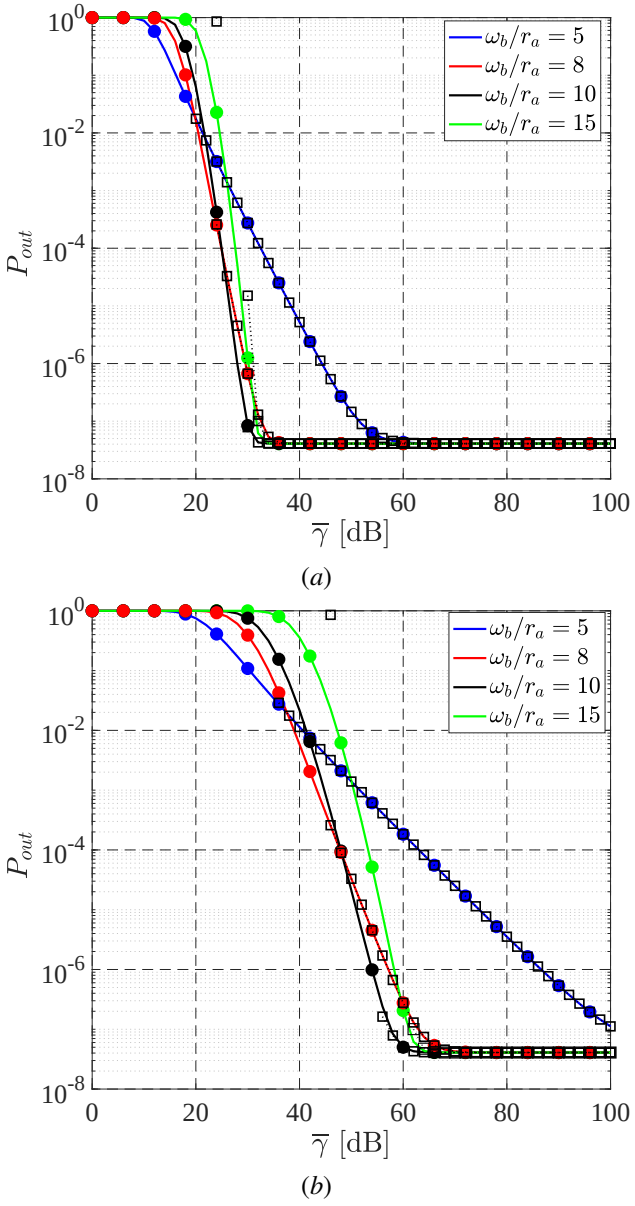

Fig. 5: OP variation versus the average SNR for different values of the beam waist ω_b, in case of (a) heterodyne and (b) IM/DD detection schemes. Circle and square markers refer to MC simulations and asymptotic trend, respectively.

that the outage performance in case of heterodyne detection outperforms those achieved with IM/DD detection scheme. Furthermore, while the OP of longer distance takes higher values, the UOWC system benefits from the IRS application for all distances. Notice that in heterodyne detection the optimal number of IRS elements to reach the outage probability of 10^{-6} for a link length of 50 m is $\mathcal{N} = 30$, while $\mathcal{N} = 12$ is the optimal value for a link length of 20 m. On the other side, for IM/DD we cannot reach an outage probability of 10^{-6} until $\mathcal{N} = 100$ elements. However, considering an outage probability of 10^{-4} the optimal number of IRS elements for a link length of 20 m is $\mathcal{N} = 60$, while $\mathcal{N} = 85$ is the optimal value for a link length of 30 m. Finally, from Fig. 2 we observe the consistency between analytical and MC simulation results that shows the accuracy of our derived results.

Fig. 3(a) and (b) depict the outage performance of an IRS-assisted UOWC link depending on the average SNR for various IRS element numbers, in case of heterodyne and IM/DD schemes, respectively. The undeniable benefit of IRS application can be seen. Using IM/DD detection scheme and keeping the average SNR as $\overline{\gamma} = 40$ dB, the OP takes the values of $\sim 7.5 \times 10^{-1}$, $\sim 1.1 \times 10^{-2}$, $\sim 4.4 \times 10^{-4}$ and $\sim 1.2 \times 10^{-4}$ for the number of IRS elements $\mathcal{N} = 1$, $\mathcal{N} = 10$, $\mathcal{N} = 50$ and $\mathcal{N} = 100$, respectively. On the other side, with heterodyne detection scheme, the OP is strongly reduced till reaching $\sim 4.23 \times 10^{-8}$ at $\overline{\gamma} = 50$ dB for $\mathcal{N} = 100$. Notice also that with heterodyne detection, the slope of the OP is faster than the curves obtained with IM/DD for a fixed number of IRS elements. Heterodyne detection benefits from the coherent detection process, which allows for the effective filtering and amplification of the signal that significantly reduce the impact of noise. The observed faster slope for heterodyne detection compared to IM/DD is primarily due to the enhanced sensitivity and superior noise rejection capabilities of heterodyne systems. This characteristic leads to a more rapid improvement in signal quality as conditions improve, thereby resulting in a faster decrease of the outage probability. Finally, for $\overline{\gamma} > 60$ dB in case of heterodyne and for $\mathcal{N} > 1$ the OP shows a flat trend at $\sim 4.1 \times 10^{-8}$. Still on the OP, Fig. 4 shows the trends of the OP depending on the misalignment of the pointing error q_H. For increasing values of q_H, the OP increases, maintaining the curves with heterodyne always lower than those achieved with IM/DD. Both the MC simulations and the asymptotic trend are in line with the OP curves, then assessing their correct behavior.

In Fig. 5, the effect of beam waist on the outage performance of IRS-assisted UOWC system is plotted. It is observed that UOWC system can benefit from beam waist up to a certain level due to increased possibility of captured irradiance by

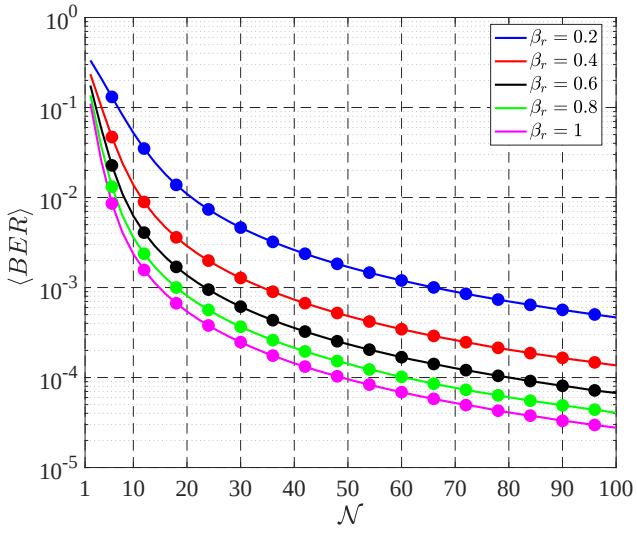

Fig. 6: Variation of the average BER for IM/DD modulated UOWC system versus the number of IRS elements, for different values of the reflection coefficient β_r. Circle markers refer to MC simulations.

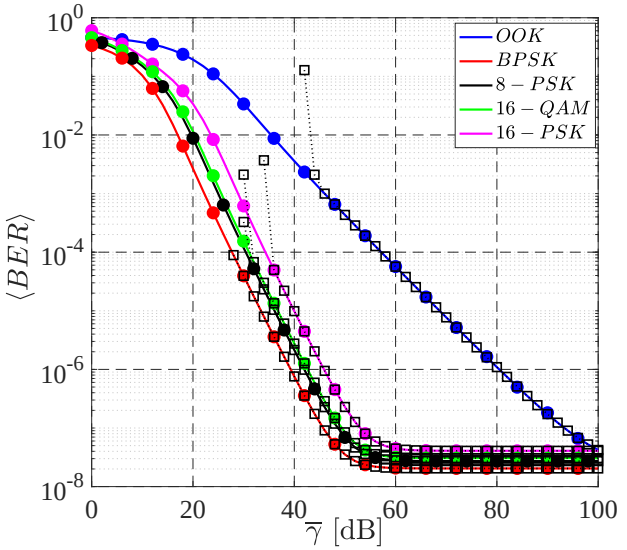

Fig. 7: Variation of the average BER versus the average SNR $\overline{\gamma}$, for different modulation schemes. Circle and square markers refer to MC simulations and asymptotic trend, respectively.

the receiver. However, a further increase causes performance degradations. Indeed, excessively large beams spread out too much, resulting in reduced intensity and more significant spreading losses at the receiver. The broader beam may also encompass more environmental noise and interference, reducing the overall signal quality and SNR. For example, in Fig. 5(*b*) for $\overline{\gamma} = 50$ dB and IM/DD detection scheme, the OP of IRS-assisted UOWC link decreases from $\sim 1.4 \times 10^{-3}$ to $\sim 2.1 \times 10^{-5}$ with the increase of beam waist from $\omega_b = 5 \times r_a$ to $\omega_b = 10 \times r_a$. However, by further increasing the beam waist to $\omega_b = 15 \times r_a$ it yields distorted performance with OP $\sim 1.4 \times 10^{-3}$ that is same with that of $\omega_b = 5 \times r_a$. This result shows that a certain level of beam waist may be useful if it can be optimized. Similar consideration apply to Fig. 5(*a*) for heterodyne detection, showing better performance than the

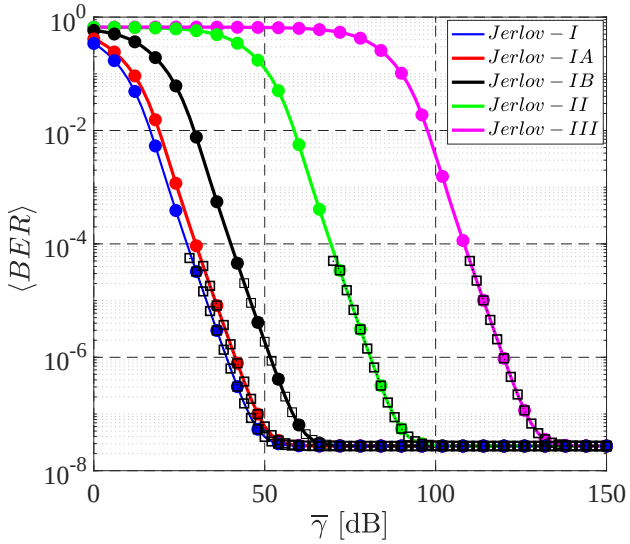

Fig. 8: Variation of the average BER for 8-phase shift keying (PSK) modulated UOWC system versus the average SNR and for different Jerlov water types, with a fixed link length *i.e.*, $L = 20$ [m]. Circle and square markers refer to MC simulations and asymptotic trend, respectively.

IM/DD case.

Fig. 6 focuses on the effects of both the number of IRS elements and the reflectivity of the surfaces on the average BER performance of IRS-assisted UOWC link for IM/DD detection scheme. Mounting an IRS equipment including $\mathcal{N} = 50$ surfaces, the average BER takes the values of $\sim 1.69 \times 10^{-3}$ and $\sim 9.56 \times 10^{-5}$ when the reflectivity of IRS elements changes from $\beta_r = 0.2$ to $\beta_r = 1$. This implies that the reflectivity of IRS elements in UOWC remains important and maximizing the reflectivity through design techniques and optimization algorithms will increase the efficiency of IRS application for overcoming the challenges associated with UOWC. Also, the higher the number of IRS elements the better performance trend is seen in Fig. 6. We compare different modulation and detection types in terms of their average BER in Fig. 7. While heterodyne detection outperforms IM/DD in all cases, the best average BER performance is obtained for binary phase shift keying (BPSK) modulation type among the selected modulation schemes. The average BER takes the values of $\sim 3.59 \times 10^{-3}$, $\sim 9.85 \times 10^{-6}$, $\sim 2.75 \times 10^{-6}$, $\sim 2.14 \times 10^{-6}$ and $\sim 7.58 \times 10^{-7}$ for on-off keying (OOK), 16-PSK, 16-quadrature amplitude modulation (QAM), 8-PSK and BPSK modulation schemes respectively when the average SNR is fixed to $\overline{\gamma} = 40$ dB. Although the best performance is obtained for BPSK modulation scheme the choice of the most appropriate modulation scheme should be carefully considered based on the implementability, the specific requirements, and the constraints of the communication system.

The variation of the average BER of IRS-assisted UOWC system using 8-PSK modulation scheme versus the average SNR is plotted in Fig. 8 for different water types. Since waters are classified according to their chlorophyll concentrations, the smallest average BER value is obtained for the water whose chlorophyll concentration is the lowest *i.e.*, Jerlov-I with the chlorophyll concentration $C_c = 0.03$ [mg/m^3]. For $\overline{\gamma} = 50$ dB,

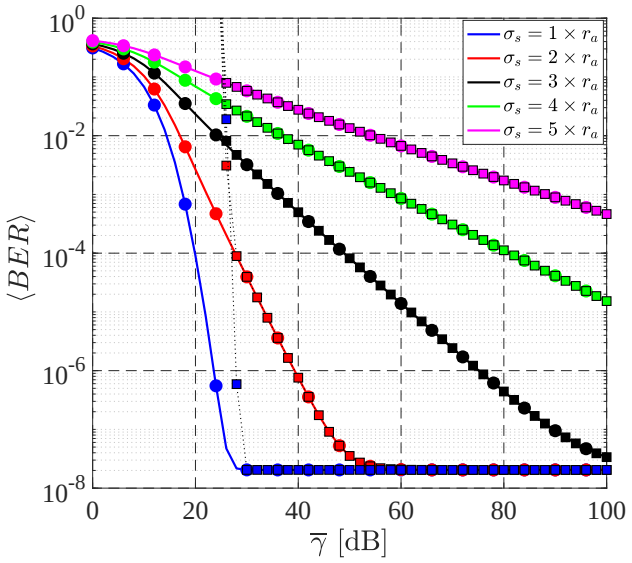

Fig. 9: Variation of the average BER for a BPSK modulated UOWC system versus the average SNR and for different beam misalignment values. Circle and square markers refer to MC simulations and asymptotic trend, respectively.

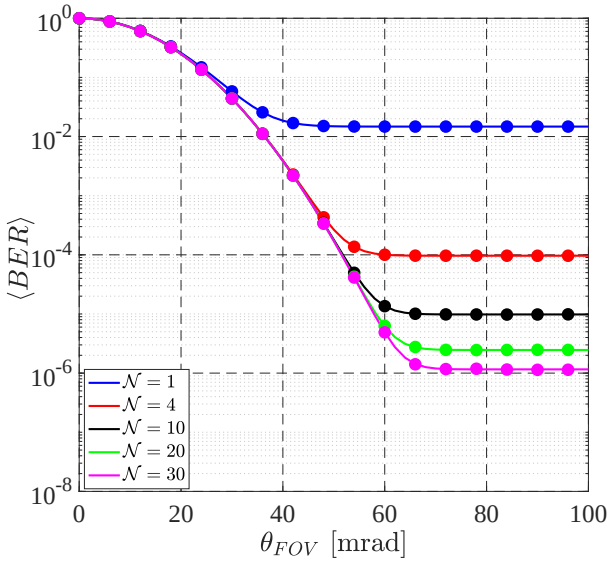

Fig. 10: Variation of the average BER variation for 16-PSK modulated UOWC system versus FoV and for different values of the IRS elements. Circle markers refer to MC simulations.

the values of average BER are $\sim 6.5 \times 10^{-1}$, $\sim 1.2 \times 10^{-1}$, $\sim 1.88 \times 10^{-6}$, $\sim 6.03 \times 10^{-8}$ and $\sim 3.94 \times 10^{-8}$ in Jerlov-III, Jerlov-II, Jerlov-IB, Jerlov-IA, and Jerlov-I waters, respectively. We observe the drastic performance destroying effect due to the strong absorption and scattering in waters with higher chloropyll concentrations (*i.e.*, Jerlov-II and Jerlov-III waters). To see the effect of pointing error on the performance of IRS assisted and BPSK modulated UOWC systems, we present Fig. 9. It is observed that the pointing error poses significant degradation to the performance of UOWC systems. As the beam misalignment increases, there is a notable decrease in the received irradiance strength and a corresponding rise in the average BER. Keeping the average SNR as $\overline{\gamma} = 40$ dB, the average BER jumps from $\sim 2 \times 10^{-8}$ to $\sim 2.7 \times 10^{-2}$ when the beam misalignment rises from $\sigma_s = 1 \times r_a$ (*blue line*) to $\sigma_s = 5 \times r_a$ (*magenta line*). This finding underscores the importance of maintaining the precise beam alignment in underwater medium to avoid pointing error-induced performance degradation.

To verify the importance of FoV, the average BER performance of a 16-PSK modulated UOWC system is presented in Fig. 10. We observe the average BER decreases with the increase of the FoV, however the performance saturates and maintains its constant values when the FoV exceeds a certain value. For instance, the average BER keeps its fixed values when $\theta_{FOV} \gtrsim 40$ mrad and $\theta_{FOV} \gtrsim 70$ mrad for $\mathcal{N} = 1$ and $\mathcal{N} = 30$ respectively. The benefit of using IRS is also seen obviously in Fig. 10, where the average BER is reduced from $\sim 1.4 \times 10^{-2}$ to $\sim 1.19 \times 10^{-6}$ with the increase of the number of IRS elements from $\mathcal{N} = 1$ to $\mathcal{N} = 30$ for the fixed value of $\theta_{FOV} = 70$ mrad, which means that it is not necessary to enlarge the FoV too much to obtain the optimum performance, instead the optimized value of FoV will be sufficient.

Fig. 11, Fig. 12 and Fig. 13 present the ergodic channel capacity of the IRS-assisted UOWC link for both heterodyne and

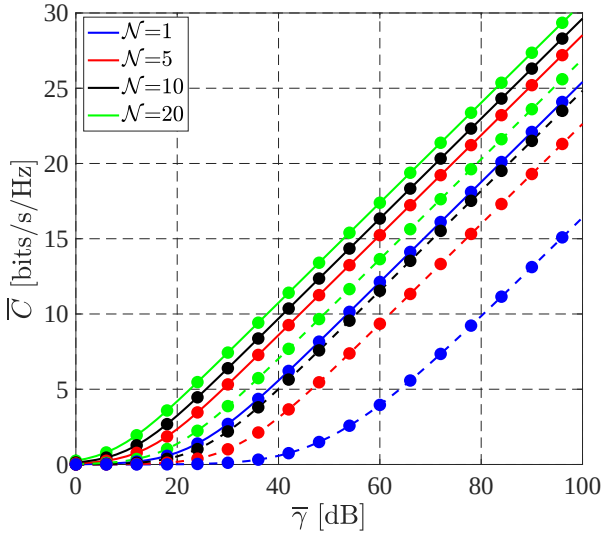

Fig. 11: Variation of the channel capacity versus the average SNR for different number of the IRS elements, in case of (*i*) IM/DD (*dashed lines*) and (*ii*) heterodyne detection schemes (*solid lines*). Circle markers refer to MC simulations.

IM/DD detection schemes depending on various parameters. In Fig. 11, keeping the average SNR at $\overline{\gamma} = 60$ dB, for IM/DD detection scheme the ergodic channel capacity varies from $\overline{C} \approx 4$ [bits/s/Hz] to $\overline{C} \approx 13.64$ [bits/s/Hz] with the increase of the number of IRS elements from $\mathcal{N} = 1$ to $\mathcal{N} = 20$, respectively. The effect of random orientation deviation resulting from AOA fluctuations on the ergodic channel capacity is given in Fig. 12. Applying heterodyne detection scheme and for $\theta_{FOV} = 20$ mrad, the increase in the orientation deviation from $\sigma_0 = 8$ mrad to $\sigma_0 = 15$ mrad yields to the ergodic channel capacity reduction from $\overline{C} \approx 9.27$ [bits/s/Hz] to $\overline{C} \approx 5.71$ [bits/s/Hz], respectively. Also, increasing the FoV angle, the channel capacity reaches its maximum value after ≈ 40 mrad, which is then maintained constant.

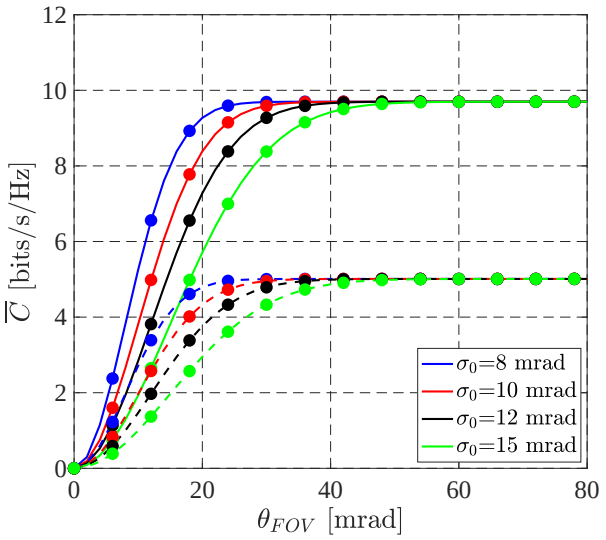

Fig. 12: Variation of the channel capacity versus the FoV for different AOA deviation, in case of (*i*) IM/DD (*dashed lines*) and (*ii*) heterodyne detection schemes (*solid lines*). Circle markers refer to MC simulations.

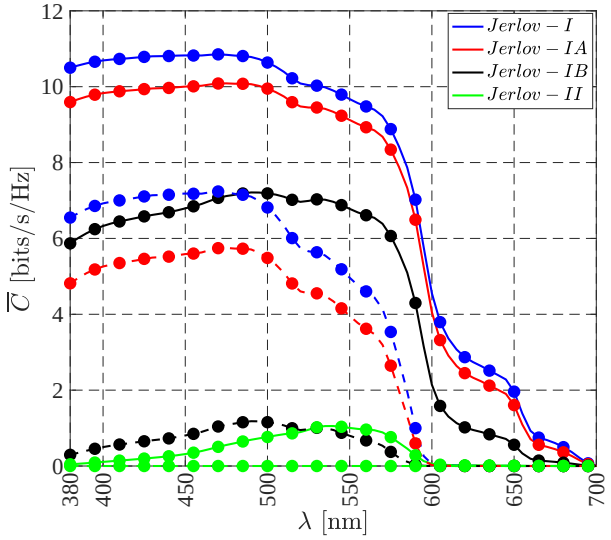

Fig. 13: Variation of the channel capacity versus wavelength for different Jerlov water types and a fixed link length (*i.e.*, $L = 20$ [m]), in case of (*i*) IM/DD (*dashed lines*) and (*ii*) heterodyne detection schemes (*solid lines*). Circle markers refer to MC simulations.

Finally, the variation of ergodic channel capacity depending on optical beam wavelength in different Jerlov water types is indicated in Fig. 13. The channel capacity takes its lowest values in Jerlov-II type water, which has the highest chlorophyll concentration. The channel capacity maintains almost at the 0 level in Jerlov-II type water for IM/DD detection scheme in all visible spectrum. Since the attenuation coefficient in underwater is strongly dependent on the wavelength [25], as well as the chlorophyll concentration, the violet, blue and green regions of the visible spectrum yield the highest channel capacity in which the absorption effect remains less when compared to other regions (*e.g.*, yellow, orange and red). For instance, using the heterodyne detection scheme and $\lambda = 420$ [nm], the ergodic channel capacity remains at higher levels in Jerlov waters (I, IA, IB and II) as $\overline{C} \approx 10.76$ [bits/s/Hz], $\overline{C} \approx 9.91$ [bits/s/Hz], $\overline{C} \approx 6.53$ [bits/s/Hz] and $\overline{C} \approx 0.17$ [bits/s/Hz] respectively.

VII. Conclusions

IRS are becoming a remarkable alternative to provide reliable communication in underwater medium in case of lack of LoS connectivity. In this study, the performance of an IRS-assisted UOWC system is investigated in terms of OP, average BER and ergodic channel capacity, under the assumption of multiple attenuation losses such as underwater optical turbulence, pointing error, and AOA fluctuations. A unified channel model is derived, working both in case of heterodyne and IM/DD mode. The analytical expressions of the channel PDF and CDF are obtained, from which we derived the analytical expressions of the average BER, OP and the ergodic channel capacity. Furthermore, we derived the asymptotic expressions of the average BER and OP. From the achieved results, it is observed first the superiority of heterodyne over IM/DD, and then that implementing IRS-aided UOWC links with a sufficient number of metasurfaces causes a significant improvement in the performance, especially for increasing values of the reflectivity factor. Results show also that the performance of an IRS-assisted UOWC system benefits from asymmetrical (when vertical and horizontal deviations are different) beam deviations rather than symmetrical case. The effect of beam waist is shown to be beneficial for IRS-assisted UOWC system up to a certain level since the probability of received irradiance falling onto photodetector increases. It is also confirmed that keeping the SNR as high as possible is crucial for underwater optical communications and the IRS application together with the higher SNR sharply improves the performance in different water types. The performance of the IRS-aided UOWC link in case of different water types is presented, showing variable trends for different wavelengths. Of course, the trade-off between the number of IRS elements and the associated computational cost should be defined to optimize the system performance. Finally, as future work, we could investigate other modulations such as the pulse position modulation (PPM), as alternative to IM/DD. Specifically, variable-weight multiple PPM (vw-MPPM) [37] is expected to provide good performance thanks to its relation to the minimum Euclidean distance among codewords.

Appendix A
Rytov Variances

The Rytov variance of Gaussian beam that is also scintillation index in weak turbulence regime is given in [28, pp.263] as

$$\sigma_B^2 = 8\pi^2 k^2 L \int_0^1 \mathrm{d}\xi \int_0^\infty \kappa \Phi_n(\kappa) \exp\left(-\frac{\Lambda_1 L \kappa^2 \xi^2}{k}\right) \times \left\{1 - \cos\left[\frac{L\kappa^2}{k}\xi(1 - \overline{\Theta}_1 \xi)\right]\right\} \mathrm{d}\kappa, \tag{A.1}$$

where ξ is the normalized distance parameter, κ is the magnitude of the spatial wave number, $k = 2\pi/\lambda$ is the wavenumber,

and $\Lambda_1 = \Lambda_0/(\Theta_0^2 + \Lambda_0^2)$ is the Gaussian beam's Fresnel ratio at the receiver. According to OTOPS turbulence power spectrum model [20], the $\Phi_n(\kappa)$ is given by

$$\Phi_n(\kappa) = A^2\Phi_T + B^2\Phi_S + 2AB\Phi_{TS}, \tag{A.2}$$

where $A = \frac{\partial n(T,S,\lambda)}{\partial T}$ and $B = \frac{\partial n(T,S,\lambda)}{\partial S}$ are the linear coefficients depending on the average temperature $\langle T\rangle$ and the average salinity concentration $\langle S\rangle$, according to $n(T,S,\lambda)$ that is the refractive index of the underwater medium. Also, Φ_T, Φ_S and Φ_{TS} denote the temperature, salinity, and co-spectra, respectively, which are given by

$$\begin{aligned}\Phi_i(\kappa) = \frac{\beta_0\varepsilon^{-1/3}\kappa^{-11/3}\chi_i}{4\pi}\left[1 + 21.61(\kappa\eta)^{0.61}c_i^{0.02}\right.\\ \left.-18.18(\kappa\eta)^{0.55}c_i^{0.04}\right]\exp\left[-174.9(\kappa\eta)^2 c_i^{0.96}\right],\end{aligned} \tag{A.3}$$

with $i \in \{T, S, TS\}$, $\beta_0 = 0.72$, ε is the energy dissipation rate, χ_T is the temperature dissipation rate, $\chi_S = d_r\chi_T/H^2$ and $\chi_{TS} = 0.5(1+d_r)\chi_T/H$ are the dissipation rates for salinity and co-spectrum, respectively. Also, d_r is the eddy diffusivity ratio, H is the temperature-salinity gradient ratio, and the c_i parameters are expressed as

$$\begin{cases} c_T = 0.072^{4/3}\beta_0 P_r^{-1} \\ c_S = 0.072^{4/3}\beta_0 S_c^{-1} \\ c_{TS} = 0.072^{4/3}\beta_0 \frac{P_r+S_c}{2P_r\cdot S_c} \end{cases}, \tag{A.4}$$

where P_r and S_c are the Prandtl and Schmidt numbers, respectively. The eddy diffusivity ratio that is used for χ_S and χ_{TS} calculation is [38]

$$d_r = \begin{cases} R_p + R_p^{0.5}\left(R_p - 1\right)^{0.5}, & R_p \geq 1, \\ 1.85R_p - 0.85, & 0.5 \leq R_p < 1, \\ 0.15R_p, & R_p < 0.5, \end{cases} \tag{A.5}$$

where $R_p = |H|\alpha_T/\beta_S$ is the density ratio, α_T is the thermal expansion coefficient, and β_S is the saline contraction coefficient. The OTOPS is a comprehensive model with many parameters working behind it. We will not go into details here due to page limitations, but it would be helpful for the readers to refer to the references [20] and [39] for further details.

Appendix B
Channel PDF Derivations

Inserting Eqs. (8) and (22) into Eq. (21), we have

$$\begin{aligned} f_{h_{ag}|\theta_d}(h_{ag}) = \frac{2\eta_s^2\left(\frac{\alpha_s\beta_s}{\mathcal{N}}\right)^{\frac{(\alpha_s+\beta_s)}{2}}}{2\pi q_H\Gamma(\alpha_s)\Gamma(\beta_s)}\int_{-\pi}^{\pi}\frac{h_{ag}^{\eta_s^2\xi(\varphi)-1}\mathrm{d}\varphi}{(A_0h_{al}\cos\theta_d)^{\eta_s^2\xi(\varphi)}} \\ \times\int_{\Delta_l}^{\infty} h_{at}^{\frac{(\alpha_s+\beta_s)}{2}-\eta_s^2\xi(\varphi)-1}K_{\alpha_s-\beta_s}\left(2\sqrt{\frac{\alpha_s\beta_s}{\mathcal{N}}h_{at}}\right)\mathrm{d}h_{at}. \end{aligned} \tag{B.1}$$

Using the conversion $K_a(x) = \frac{1}{2}\mathrm{G}_{0,2}^{2,0}\left(\frac{x^2}{4}\middle|\begin{matrix}-\\ a/2,-a/2\end{matrix}\right)$ [40, Eq.(14)] and then applying [41, Eq.(07.34.21.0085.01)] to take h_{at} dependent integral then applying [41, Eq.(07.34.17.0011.01)] for simplification, Eq. (B.1) becomes

$$\begin{aligned} f_{h_{ag}|\theta_d}(h_{ag}) = \frac{\eta_s^2 h_{ag}^{-1}}{2\pi q_H\Gamma(\alpha_s)\Gamma(\beta_s)} \\ \times\int_{-\pi}^{\pi} G_{1,3}^{3,0}\left(\frac{\alpha_s\beta_s h_{ag}}{\mathcal{N}A_0h_{al}\cos\theta_d}\middle|\begin{matrix}1+\eta_s^2\xi(\varphi)\\ \eta_s^2\xi(\varphi),\alpha_s,\beta_s\end{matrix}\right)\mathrm{d}\varphi. \end{aligned} \tag{B.2}$$

Then, the PDF of the combined total effective channel can be calculated by using

$$f_h(h) = \int_0^{\infty} h_{af}f_{h_{ag}|\theta_d}(h)f_{\theta_d}(\theta_d)\mathrm{d}\theta_d. \tag{B.3}$$

Since h_{af} takes the discrete values of "1" and "0" as given in Eq. (14), the PDF of the total channel state can be expressed in two parts as

$$f_h(h) = \int_0^{\theta_{FOV}} f_{h_{ag}|\theta_d}(h)f_{\theta_d}(\theta_d)\mathrm{d}\theta_d + \delta(h)\int_{\theta_{FOV}}^{\infty} f_{\theta_d}(\theta_d)\mathrm{d}\theta_d, \tag{B.4}$$

where the first and second terms reflect the effects of AOA within and outside of the receiver's FoV, respectively [42], $\delta(\cdot)$ is the impulse function and $\delta(h)$ accounts for any possible non-zero contributions in case of $h_{af} \approx 0$. On substituting Eqs. (15) and (B.2)) into Eq. (B.4), we obtain:

$$\begin{aligned} f_h(h) = \frac{\eta_s^2 h^{-1}}{2\pi q_H\Gamma(\alpha_s)\Gamma(\beta_s)} \\ \times\int_{-\pi}^{\pi} G_{1,3}^{3,0}\left(\frac{\alpha_s\beta_s h}{\mathcal{N}A_0h_{al}\cos\theta_d}\middle|\begin{matrix}1+\eta_s^2\xi(\varphi)\\ \eta_s^2\xi(\varphi),\alpha_s,\beta_s\end{matrix}\right)\mathrm{d}\varphi \\ \times\int_0^{\theta_{FOV}}\frac{\theta_d}{\sigma_0^2}e^{-\frac{\theta_d^2}{2\sigma_0^2}}\mathrm{d}\theta_d + \delta(h)\int_{\theta_{FOV}}^{\infty}\frac{\theta_d}{\sigma_0^2}e^{-\frac{\theta_d^2}{2\sigma_0^2}}\mathrm{d}\theta_d. \end{aligned} \tag{B.5}$$

Using small angle approximation *i.e.*, $\cos\theta_d \approx 1$, and then applying [43, Eq.(3.381-8)] to the first θ_d dependent integral, and then applying [43, Eq.(3.381-9)] to the second θ_d dependent integral in Eq. (B.5), the PDF of the effective channel will be obtained as given in Eq. (23).

Appendix C
Channel CDF Derivations

Inserting Eq. (25) into Eq. (26), we have

$$\begin{aligned} F_\gamma(\gamma) = \frac{\eta_s^2\left[1-\exp\left(-\theta_{FOV}^2/2\sigma_0^2\right)\right]}{r2\pi q_H\Gamma(\alpha_s)\Gamma(\beta_s)}\int_{-\pi}^{\pi}\mathrm{d}\varphi \\ \times\underbrace{\int_0^{\gamma} x^{-1}G_{1,3}^{3,0}\left[\frac{\alpha\beta(x/\overline{\gamma})^{\frac{1}{r}}}{\mathcal{N}A_0h_{al}}\middle|\begin{matrix}1+\eta_s^2\xi(\varphi)\\ \eta_s^2\xi(\varphi),\alpha,\beta\end{matrix}\right]\mathrm{d}x}_{\mathcal{I}_1} \\ +e^{-\frac{\theta_{FOV}^2}{2\sigma_0^2}}\underbrace{\int_0^{\gamma}\frac{\delta\left[(x/\overline{\gamma})^{\frac{1}{r}}\right]}{r\overline{\gamma}^{\frac{1}{r}}x^{1-\frac{1}{r}}}\mathrm{d}x}_{\mathcal{I}_2}. \end{aligned} \tag{C.1}$$

Converting variables as $t = x^{\frac{1}{r}}$ and applying [40, Eq.(26)] for $\mathcal{I}_1$, and moreover, applying variable conversion as $t = (x/\overline{\gamma})^{\frac{1}{r}}$ for $\mathcal{I}_2$ will yield the CDF of instantaneous SNR as given in Eq. (27).

APPENDIX D
AVERAGE BER DERIVATIONS

Inserting the unified channel PDF in Eq. (25) into Eq. (30)

$$P_e = \frac{\delta_x \eta_s^2 \left[1 - \exp\left(-\theta_{FOV}^2/2\sigma_0^2\right)\right]}{r 4\pi q_H \Gamma(\alpha_s)\Gamma(\beta_s)\Gamma(p)} \int_{-\pi}^{\pi} \mathrm{d}\varphi \sum_{l=1}^{n_x} \times \underbrace{\int_0^{\infty} \gamma^{-1}\Gamma(p, q_l\gamma) G_{1,3}^{3,0}\left[\Delta_a \middle| \begin{matrix} 1+\eta_s^2\xi(\varphi) \\ \eta_s^2\xi(\varphi), \alpha_s, \beta_s \end{matrix}\right] \mathrm{d}\gamma}_{\mathcal{I}_3} + \frac{\delta_x \exp\left(-\theta_{FOV}^2/2\sigma_0^2\right)}{2\Gamma(p) r \overline{\gamma}^{\frac{1}{r}}} \sum_{l=1}^{n_x} \underbrace{\int_0^{\infty} \frac{\Gamma(p, q_l\gamma)}{\gamma^{1-\frac{1}{r}}} \delta(\Delta_b) \mathrm{d}\gamma}_{\mathcal{I}_4} \tag{D.1}$$

where $\Delta_a = \frac{\alpha_s \beta_s \gamma^{\frac{1}{r}}}{\mathcal{N} A_0 h_{al} \overline{\gamma}^{\frac{1}{r}}}$ and $\Delta_b = (\gamma/\overline{\gamma})^{\frac{1}{r}}$. For $\mathcal{I}_4$, changing variable as $x = (\gamma/\overline{\gamma})^{\frac{1}{r}}$ and using $\int_0^{\infty} \delta(x) f(x) dx = f(0)$ for $\delta(.)$ function, Eq. (D.1) becomes

$$P_e = \frac{\delta_x n_x}{2\Gamma(p)} e^{-\frac{\theta_{FOV}^2}{2\sigma_0^2}} + \frac{\delta_x \eta_s^2 \left[1 - \exp\left(-\theta_{FOV}^2/2\sigma_0^2\right)\right]}{r 4\pi q_H \Gamma(\alpha_s)\Gamma(\beta_s)\Gamma(p)} \times \int_{-\pi}^{\pi} \mathrm{d}\varphi \sum_{l=1}^{n_x} \underbrace{\int_0^{\infty} \frac{\Gamma(p, q_l\gamma)}{\gamma} G_{1,3}^{3,0}\left[\Delta_a \middle| \begin{matrix} 1+\eta_s^2\xi(\varphi) \\ \eta_s^2\xi(\varphi), \alpha_s, \beta_s \end{matrix}\right] \mathrm{d}\gamma}_{\mathcal{I}_3}. \tag{D.2}$$

According to [41, Eq.(06.06.26.0005.01)], the upper incomplete Gamma function in Eq. (D.2) can be written in terms of Meijer-G function as $\Gamma(p, q_l\gamma) = G_{1,2}^{2,0}\left(q_l\gamma \middle| \begin{matrix} 1 \\ 0, p \end{matrix}\right)$. Inserting this expression into Eq. (D.2) and then applying [41, Eq.(07.34.21.0013.01)], the average BER expression including both heterodyne and IM/DD detection schemes can be found as given in Eq. (31).

APPENDIX E
CHANNEL CAPACITY DERIVATIONS

By inserting the unified channel PDF expressed in Eq. (25) into Eq. (32), we get

$$\overline{C} = \frac{\eta_s^2 \left[1 - \exp\left(-\theta_{FOV}^2/2\sigma_0^2\right)\right]}{r 2 \ln 2 \pi q_H \Gamma(\alpha_s)\Gamma(\beta_s)} \int_{-\pi}^{\pi} \mathrm{d}\varphi \times \underbrace{\int_0^{\infty} \frac{\ln(1+c_r\gamma)}{\gamma} G_{1,3}^{3,0}\left[\Delta_a \middle| \begin{matrix} 1+\eta_s^2\xi(\varphi) \\ \eta_s^2\xi(\varphi), \alpha_s, \beta_s \end{matrix}\right] \mathrm{d}\gamma}_{\mathcal{I}_5} + \frac{1}{\ln 2} \exp\left(-\frac{\theta_{FOV}^2}{2\sigma_0^2}\right) \underbrace{\int_0^{\infty} \frac{\ln(1+c_r\gamma)}{r\overline{\gamma}^{\frac{1}{r}}\gamma^{1-\frac{1}{r}}} \delta(\Delta_b) \mathrm{d}\gamma}_{\mathcal{I}_6}. \tag{E.1}$$

To solve integral $\mathcal{I}_6$ in Eq. (E.1), changing variables as $x = (\gamma/\overline{\gamma})^{\frac{1}{r}}$ and then using the $\int_0^{\infty} \delta(x) f(x) = f(0)$ for Dirac delta function will yield $\mathcal{I}_6 = 0$ and Eq. (E.1) becomes

$$\overline{C} = \frac{\eta_s^2 \left[1 - \exp\left(-\theta_{FOV}^2/2\sigma_0^2\right)\right]}{r 2 \ln 2 \pi q_H \Gamma(\alpha_s)\Gamma(\beta_s)} \int_{-\pi}^{\pi} \mathrm{d}\varphi \times \underbrace{\int_0^{\infty} \frac{\ln(1+c_r\gamma)}{\gamma} G_{1,3}^{3,0}\left[\Delta_b \middle| \begin{matrix} 1+\eta_s^2\xi(\varphi) \\ \eta_s^2\xi(\varphi), \alpha_s, \beta_s \end{matrix}\right] \mathrm{d}\gamma}_{\mathcal{I}_5}. \tag{E.2}$$

According to [40, Eq.(11)], the logarithmic term in integral $\mathcal{I}_5$ of Eq. (E.2) can be expressed through Meijer-G function as

$$\ln(1+c_r\gamma) = G_{2,2}^{1,2}\left(c_r\gamma \middle| \begin{matrix} 1, 1 \\ 1, 0 \end{matrix}\right). \tag{E.3}$$

Inserting Eq. (E.3) into Eq. (E.2), then using [41, Eq.(07.34.21.0013.01)] with tedious calculations, the ergodic channel capacity for UOWC link can be obtained as given in Eq. (33).

APPENDIX F
ASYMPTOTIC DERIVATIONS

A. Outage Probability

According to [44, pp.9], a relationship between H-and Meijer-G function is given as

$$H_{p,q}^{m,n}\left(z \middle| \begin{matrix} (a_1, C), \ldots, (a_p, C) \\ (b_1, C), \ldots, (b_q, C) \end{matrix}\right) = \frac{1}{C} G_{p,q}^{m,n}\left(z^{\frac{1}{C}} \middle| \begin{matrix} a_1, \ldots, a_p \\ b_1, \ldots, b_q \end{matrix}\right). \tag{F.1}$$

Then, the OP in Eq. (29) can be expressed by

$$P_{out} = \frac{\eta_s^2 \left[1 - \exp\left(-\theta_{FOV}^2/2\sigma_0^2\right)\right]}{2\pi q_H \Gamma(\alpha_s)\Gamma(\beta_s)} \int_{-\pi}^{\pi} \mathrm{d}\varphi \times H_{2,4}^{3,1}\left[\frac{\alpha_s \beta_s \gamma_{th}^{\frac{1}{r}}}{\mathcal{N} A_0 h_{al} \overline{\gamma}^{\frac{1}{r}}} \middle| \begin{matrix} (1,1), (1+\eta_s^2\xi(\varphi), 1) \\ (\eta_s^2\xi(\varphi), 1), (\alpha_s, 1), (\beta_s, 1), (0, 1) \end{matrix}\right] + \exp\left(-\frac{\theta_{FOV}^2}{2\sigma_0^2}\right). \tag{F.2}$$

It is shown in [45, pp.19] that the asymptotic expansion of H-function can be obtained by

$$H_{p,q}^{m,n}\left[z \middle| \begin{matrix} (a_i, \alpha_i)_{1,p} \\ (b_i, \beta_i)_{1,q} \end{matrix}\right] = \sum_{j=1}^{m} h_j^* z^{\frac{b_j}{\beta_j}}, \quad z \to 0 \tag{F.3}$$

while h_j^* coefficients are

$$h_j^* = \frac{1}{\beta_j} \frac{\prod_{\substack{i=1 \\ i \neq j}}^{m} \Gamma\left(b_i - b_j \frac{\beta_i}{\beta_j}\right) \prod_{i=1}^{n} \Gamma\left(1 - a_i + b_j \frac{\alpha_i}{\beta_j}\right)}{\prod_{i=n+1}^{p} \Gamma\left(a_i - b_j \frac{\alpha_i}{\beta_j}\right) \prod_{i=m+1}^{q} \Gamma\left(1 - b_i + b_j \frac{\beta_i}{\beta_j}\right)}. \tag{F.4}$$

Applying Eqs. (F.4) and (F.3) to Eq. (F.2), the asymptotic expansion of OP is obtained as given in Eq. (34).

$$P_e = \frac{r^{\alpha_s+\beta_s-3}\delta_x\eta_s^2\left[1-\exp\left(-\theta_{FOV}^2/2\sigma_0^2\right)\right]}{2(2\pi)^r q_H \Gamma(\alpha_s)\Gamma(\beta_s)\Gamma(p)} \int_{-\pi}^{\pi} \mathrm{d}\varphi \sum_{l=1}^{n_x} \times H_{r+2,3r+1}^{3r,2}\left(\Delta_y \middle| \begin{matrix}(1,\frac{1}{r}),(1-p,\frac{1}{r}),[\Delta(1+\eta_s^2\xi(\varphi):r),\frac{1}{r}] \\ [\Delta(\eta_s^2\xi(\varphi):r),\frac{1}{r}],[\Delta(\alpha_s:r),\frac{1}{r}],[\Delta(\beta_s:r),\frac{1}{r}],(0,\frac{1}{r})\end{matrix}\right) + \frac{n_x\delta_x}{2} e^{-\frac{\theta_{FOV}^2}{2\sigma_0^2}}. \tag{F.5}$$

B. Average BER

Using Eq. (F.1), Eq. (31) can be written as given in Eq. (F.5). Then, using the following structure

$$H_{p,q}^{m,n}\left[z\middle|\begin{matrix}(a_i,\alpha_i)_{1,p}\\(b_i,\beta_i)_{1,q}\end{matrix}\right] = \sum_{j=1}^{m} h_j^{\dagger}\Delta_y^{\frac{b_j}{\beta_j}}, \quad \Delta_y \to 0, \tag{F.6}$$

where $\Delta_y = [\alpha\beta/(A_0 h_{al} r^2 \mathcal{N} q_l^{\frac{1}{r}}\overline{\gamma}^{\frac{1}{r}})]$, according to Eq. (F.5) it can be seen that the parameters in Eq. (F.6) are expressed as

$$a_1, a_2, \ldots, a_{r+2} = 1, 1-p, \ldots, \Delta(1+\eta_s^2\xi(\varphi):r), \tag{F.7}$$

$$b_1, b_2, \ldots, b_{3r+1} = \Delta(\eta_s^2\xi(\varphi):r), \Delta(\alpha_s:r), \Delta(\beta_s:r), \ldots, 0, \tag{F.8}$$

$$\alpha_1, \ldots, \alpha_{r+2} = \beta_1, \ldots, \beta_{3r+1} = \frac{1}{r}, \tag{F.9}$$

and

$$h_j^{\dagger} = r\frac{\prod_{\substack{i=1\\i\neq j}}^{3r}\Gamma(b_i-b_j)\prod_{i=1}^{2}\Gamma(1-a_i+b_j)}{\prod_{i=3}^{r+2}\Gamma(a_i-b_j)\prod_{i=3r+1}^{3r+1}\Gamma(1-b_i+b_j)}. \tag{F.10}$$

Following the above aforementioned equations, the asymptotic expansion of average BER is found as given in Eq. (39).

ACKNOWLEDGMENT

This article was based upon work from COST Action NEWFOCUS CA19111, supported by COST (European Cooperation in Science and Technology). It was also partially supported by PRIN 2022 LAGO-ON (opticaL wireless undewAter positioninG for marine mOnitOriNg) project, funded by the Italian Ministry of University and Research.

REFERENCES

[1] C. Liaskos, S. Nie, A. Tsioliaridou, A. Pitsillides, S. Ioannidis, and I. Akyildiz, "A new wireless communication paradigm through software-controlled metasurfaces," *IEEE Communications Magazine*, vol. 56, no. 9, pp. 162–169, 2018.

[2] Q. Wu and R. Zhang, "Towards smart and reconfigurable environment: Intelligent reflecting surface aided wireless network," *IEEE Communications Magazine*, vol. 58, no. 1, pp. 106–112, 2020.

[3] M. Di Renzo, M. Debbah, D.-T. Phan-Huy, A. Zappone, M.-S. Alouini, C. Yuen, V. Sciancalepore, G. C. Alexandropoulos, J. Hoydis, H. Gacanin *et al.*, "Smart radio environments empowered by reconfigurable AI meta-surfaces: An idea whose time has come," *EURASIP Journal on Wireless Communications and Networking*, vol. 2019, no. 1, pp. 1–20, 2019.

[4] E. Basar, "Transmission through large intelligent surfaces: a new frontier in wireless communications," in *2019 European Conference on Networks and Communications (EuCNC)*. IEEE, 2019, pp. 112–117.

[5] E. Basar, M. Di Renzo, J. De Rosny, M. Debbah, M.-S. Alouini, and R. Zhang, "Wireless communications through reconfigurable intelligent surfaces," *IEEE Access*, vol. 7, pp. 116 753–116 773, 2019.

[6] R. Karasik, O. Simeone, M. Di Renzo, and S. S. Shitz, "Beyond max-SNR: Joint encoding for reconfigurable intelligent surfaces," in *2020 IEEE International Symposium on Information Theory (ISIT)*. IEEE, 2020, pp. 2965–2970.

[7] M. Di Renzo, K. Ntontin, J. Song, F. H. Danufane, X. Qian, F. Lazarakis, J. De Rosny, D.-T. Phan-Huy, O. Simeone, R. Zhang *et al.*, "Reconfigurable intelligent surfaces vs. relaying: Differences, similarities, and performance comparison," *IEEE Open Journal of the Communications Society*, vol. 1, pp. 798–807, 2020.

[8] L. Yang, Y. Yang, M. O. Hasna, and M.-S. Alouini, "Coverage, probability of SNR gain, and DOR analysis of RIS-aided communication systems," *IEEE Wireless Communications Letters*, vol. 9, no. 8, pp. 1268–1272, 2020.

[9] V. Jamali, H. Ajam, M. Najafi, B. Schmauss, R. Schober, and H. V. Poor, "Intelligent reflecting surface assisted free-space optical communications," *IEEE Communications Magazine*, vol. 59, pp. 57–63, 2021. [Online]. Available: https://api.semanticscholar.org/CorpusID:235212141

[10] M. Najafi, B. Schmauss, and R. Schober, "Intelligent reflecting surfaces for free space optical communication systems," *IEEE Transactions on Communications*, vol. 69, no. 9, pp. 6134–6151, 2021.

[11] L. Han, X. Liu, Y. Wang, and X. Hao, "Analysis of RIS-assisted FSO systems over $\mathcal{F}$-turbulence channel with pointing errors and imperfect CSI," *IEEE Wireless Communications Letters*, vol. 11, no. 9, pp. 1940–1944, 2022.

[12] J. Sipani, P. Sharda, and M. R. Bhatnagar, "Modeling and Design of IRS-Assisted FSO System Under Random Misalignment," *IEEE Photonics Journal*, vol. 15, no. 4, pp. 1–13, 2023.

[13] G. Xu and J. Lai, "Average capacity analysis of the underwater optical plane wave over anisotropic moderate-to-strong oceanic turbulence channels with the Malaga fading model," *Opt. Express*, vol. 28, no. 16, pp. 24 056–24 068, Aug 2020. [Online]. Available: https://opg.optica.org/oe/abstract.cfm?URI=oe-28-16-24056

[14] W. Liu, Z. Xu, and L. Yang, "SIMO detection schemes for underwater optical wireless communication under turbulence," *Photonics Research*, vol. 3, no. 3, pp. 48–53, 2015.

[15] K. O. Odeyemi, P. A. Owolawi, and O. O. Olakanmi, "Performance analysis of reconfigurable intelligent surface assisted underwater optical communication system," *Progress In Electromagnetics Research M*, vol. 98, pp. 101–111, 2020.

[16] S. Kisseleff, S. Chatzinotas, and B. Ottersten, "Reconfigurable intelligent surfaces in challenging environments: Underwater, underground, industrial and disaster," *IEEE Access*, vol. 9, pp. 150 214–150 233, 2021.

[17] R. P. Naik and W.-Y. Chung, "Evaluation of reconfigurable intelligent surface-assisted underwater wireless optical communication system," *Journal of Lightwave Technology*, vol. 40, no. 13, pp. 4257–4267, 2022.

[18] S. Tang, Y. Dong, and X. Zhang, "Impulse Response Modeling for Underwater Wireless Optical Communication Links," *IEEE Transactions on Communications*, vol. 62, no. 1, pp. 226–234, 2014.

[19] Y. Ata, H. Abumarshoud, L. Bariah, S. Muhaidat, and M. A. Imran, "Intelligent reflecting surfaces for underwater visible light communications," *IEEE Photonics Journal*, vol. 15, no. 1, pp. 1–10, 2023.

[20] J.-R. Yao, M. Elamassie, and O. Korotkova, "Spatial power spectrum of natural water turbulence with any average temperature, salinity concentration, and light wavelength," *JOSA A*, vol. 37, no. 10, pp. 1614–1621, 2020.

[21] V. T. Lam, D. T. Anh, N. Van Thang, T. D. Sy, and D. T. Ngoc, "Outage Performance of IRS-Assisted Underwater Optical Wireless Communication Systems over Combined Channel Model," in *2023 19th International Conference on Wireless and Mobile Computing, Networking and Communications (WiMob)*, 2023, pp. 318–323.

[22] Y. Ata, M. C. Gökçe, and Y. Baykal, "Intelligent reflecting surface aided vehicular optical wireless communication systems using higher-order mode in underwater channel," *IEEE Transactions on Vehicular Technology*, pp. 1–13, 2024.
[23] H. M. Oubei, E. Zedini, R. T. ElAfandy, A. Kammoun, T. K. Ng, M.-S. Alouini, and B. S. Ooi, "Efficient Weibull channel model for salinity induced turbulent underwater wireless optical communications," in *2017 Opto-Electronics and Communications Conference (OECC) and Photonics Global Conference (PGC)*, 2017, pp. 1–2.
[24] V. I. Haltrin, "Chlorophyll-based model of seawater optical properties," *Applied Optics*, vol. 38, no. 33, pp. 6826–6832, 1999.
[25] A. Morel and L. Prieur, "Analysis of variations in ocean color 1," *Limnology and Oceanography*, vol. 22, no. 4, pp. 709–722, 1977.
[26] N. G. Jerlov, *Marine Optics*. Elsevier, 1976.
[27] P. Salcedo-Serrano, R. Boluda-Ruiz, J. M. Garrido-Balsells, and A. García-Zambrana, "On the scattering-induced fading for optical wireless links through seawater: statistical characterization and its applications," *Optics Express*, vol. 29, no. 23, pp. 37 101–37 116, 2021.
[28] L. C. Andrews and R. L. Phillips, "Laser beam propagation through random media," *Laser Beam Propagation Through Random Media: Second Edition*, 2005.
[29] N. D. Chatzidiamantis and G. K. Karagiannidis, "On the distribution of the sum of Gamma-Gamma variates and applications in RF and optical wireless communications," *IEEE Transactions on Communications*, vol. 59, no. 5, pp. 1298–1308, 2011.
[30] W. Gappmair, S. Hranilovic, and E. Leitgeb, "OOK performance for terrestrial FSO links in turbulent atmosphere with pointing errors modeled by hoyt distributions," *IEEE Communications Letters*, vol. 15, no. 8, pp. 875–877, 2011.
[31] A. Jurado-Navas, J. M. Garrido-Balsells, J. F. Paris, and A. Puerta-Notario, "A Unifying Statistical Model for Atmospheric Optical Scintillation," in *Numerical Simulations of Physical and Engineering Processes*, J. Awrejcewicz, Ed. Rijeka: IntechOpen, 2011, ch. 8. [Online]. Available: https://doi.org/10.5772/25097
[32] R. Gagliardi and S. Karp, *Optical Communications*. Wiley Inter-Science, New York, 1995.
[33] H. Safi, A. Dargahi, J. Cheng, and M. Safari, "Analytical channel model and link design optimization for ground-to-HAP free-space optical communications," *IEEE/OSA Journal of Lightwave Technology*, vol. 38, no. 18, pp. 5036–5047, 2020.
[34] E. Zedini, H. Soury, and M.-S. Alouini, "Dual-hop FSO transmission systems over Gamma–Gamma turbulence with pointing errors," *IEEE Transactions on Wireless Communications*, vol. 16, no. 2, pp. 784–796, 2016.
[35] A. Lapidoth, S. M. Moser, and M. A. Wigger, "On the capacity of free-space optical intensity channels," *IEEE Transactions on Information Theory*, vol. 55, no. 10, pp. 4449–4461, 2009.
[36] G. Stratidakis, S. Droulias, and A. Alexiou, "Impact of Reconfigurable Intelligent Surface size on beamforming efficiency," in *2021 IEEE 32nd Annual International Symposium on Personal, Indoor and Mobile Radio Communications (PIMRC)*, 2021, pp. 1–5.
[37] J. Garrido-Balsells, A. Garcia-Zambrana, and A. Puerta-Notario, "Variable weight MPPM technique for rate-adaptive optical wireless communications," *Electronics Letters*, vol. 42, pp. 43–4, 02 2006.
[38] M. Elamassie, M. Uysal, Y. Baykal, M. Abdallah, and K. Qaraqe, "Effect of eddy diffusivity ratio on underwater optical scintillation index," *JOSA A*, vol. 34, no. 11, pp. 1969–1973, 2017.
[39] Y. Ata, J. Yao, and O. Korotkova, "BER variation of an optical wireless communication system in underwater turbulent medium with any temperature and salinity concentration," *Optics Communications*, vol. 485, p. 126751, 2021. [Online]. Available: https://www.sciencedirect.com/science/article/pii/S0030401821000018
[40] V. Adamchik and O. Marichev, "The algorithm for calculating integrals of hypergeometric type functions and its realization in REDUCE system," in *Proceedings of the International Symposium on Symbolic and Algebraic Computation*, 1990, pp. 212–224.
[41] W. Inc., "The wolfram functions site," 2024, last accessed 29 January 2024. [Online]. Available: https://functions.wolfram.com
[42] S. Huang and M. Safari, "Free-space optical communication impaired by angular fluctuations," *IEEE Transactions on Wireless Communications*, vol. 16, no. 11, pp. 7475–7487, 2017.
[43] I. S. Gradshteyn and I. M. Ryzhik, *Table of integrals, series, and products*. Academic Press, 2014.
[44] C. A. Coelho and B. C. Arnold, *Finite form representations for Meijer G and fox H functions*. Springer, 2019.
[45] A. A. Kilbas, *H-transforms: Theory and Applications*. CRC press, 2004.